Electrochemical Formation of C-S Bonds from CO_2 and Small Molecule Sulfur Species

Junnan Li,[a,1] Hasan Al-Mahayni,[b,1] Daniel Chartrand,[a] Ali Seifitokaldani,[b*] and Nikolay Kornienko[a*]

[1]Equal contribution

[a]Department of Chemistry, Université de Montréal, 1375 Ave. Thérèse-Lavoie-Roux, Montréal, QC H2V 0B3

[b]Department of Chemical Engineering, McGill University, 3610 University Street, Montréal, H3A 0C5 Québec, Canada

[*]Correspondence to: ali.seifitokaldani@mcgill.ca and nikolay.kornienko@umontreal.ca

Abstract

The formation of C-S bonds is an important step in the synthesis of pharmaceutical, biological, and chemical products. A very attractive green route to C-S bond containing species would be one driven through electrocatalysis using abundant small molecule precursors but examples within this context are largely absent from the literature. To this end, this work demonstrates the use of CO_2 and SO_3^{2-} as cheap building blocks that couple on the surface Cu-based heterogeneous catalysts to form hydroxymethanesulfonate, sulfoacetate and methanesulfonate for the first time, with Faradaic efficiencies of up to 9.5%. A combination of *operando* measurements and computational modelling reveal that *CHOH formed on metallic Cu is a key electrophilic intermediate that is nucleophilically attacked by SO_3^{2-} in the principal C-S bond forming step. In all, the proof-of-concept for electrocatalytic C-S bond formation and mechanistic insights gained stand to substantially broaden the scope of the emerging field of electrosynthesis.

Introduction

In light of the ever-growing consequences of fossil fuel consumption, the development of green, low-emitting technologies like electrosynthesis is becoming increasingly important. The last decades of work in this field have focused on water electrolysis[1] to produce H_2 as an energy vector and chemical feedstock as well as CO_2 reduction[2,3] to generate carbon-based fuels and commodity chemicals. However, these two classes of products do not fully meet the needs of society and the chemical industry. Against this backdrop, a recent push in the field of electrocatalysis has been to expand the scope of products that can be generated from abundant building blocks (e.g. CO_2, N_2, H_2O…)[4] and this includes directions such as H_2O_2 electrosynthesis from water and O_2,[5] N_2 reduction for NH_3 production,[6] and the formation of products with C-N bonds.[7]

Despite sulfur's abundance on earth and the importance of molecules with C-S bonds in biology,[8,9] pharma,[10] agriculture,[11] battery technologies[12] and optoelectronic materials,[13] the electrosynthesis of such species remains unexplored. Though the organic chemistry of C-S bond formation is established with strategies such as Diels-Alder reactions,[14] allylic or methane sulfonation[15,16] and sulfa-Michael addition[17], they face limitations of complex synthetic methodology, toxic byproducts/solvents and scalability limits thus hampering their sustainable implementation in the chemical industry at large. In contrast, renewable energy-driven routes have begun to be explored with photochemical C-S bond formation as an example that has been attained with carbon nitride photocatalysts in which C-S coupling occurred through radical-based routes[18] or through the addition of H_2S onto C=N bonds.[19] Methane sulfonation under high pressure conditions, presumably through radical-based C-S coupling in the electrolyte, has also begun to be explored.[20] However, direct electrochemical C-S bond coupling under ambient conditions using starting reactants like CO_2, is still to be realized.

Recently, our lab and others in the field has shown the capacity for electrochemical C-N bond generation using CO_2 and small molecule N-sources (e.g. N_2, NO_3^-, NO_2^-, NH_3…).[21-24] These reactions primarily proceeded through the reduction of CO_2 to form an activated electrophilic intermediate and subsequent coupling with a (near-)surface N-containing nucleophile. This extension of electrochemical routes enabled the build-up of higher-value, complex products than those simply available through CO_2 reduction. With this in mind, we hypothesized that C-S coupling should also be possible through a similar pathway as sulfur and nitrogen should have similar properties from the diagonal relationships found within the periodic table.[25] Thus, we moved to translate our methodology to C-S bond formation in a similar reaction setup. As a starting point, we used Cu-based catalysts[26] as a model system to generate activated electrophilic intermediates from CO_2 and SO_3^{2-} as a representative S-based nucleophile (Fig. 1). Doing so, we established new reaction pathways to hydroxymethane sulfonate (HMS), sulfoacetate (SA) and methane sulfonate (MS) products via electrochemical C-S coupling with up to 9.5% Faradaic efficiency (FE). These products have use as cement additives and membrane components (SA),[27,28] electrolytes and agents in organic synthesis (MS),[29-31] and within various facets of the textile industry (HMS).[32]

To investigate the reaction pathway and extract out mechanistic insights translatable to future works, we carried out a combination of *operando* experiments (performed while the reaction was occurring) and computation modelling which pointed to *CHOH coupling to SO_3^{2-} as a likely rate-limiting step. Crucially, this work introduces C-S bond formation in an expansion of the scope of sustainable electrosynthesis and opens up potential avenues for C-S chemical production from abundant sources and powered via renewable electricity.

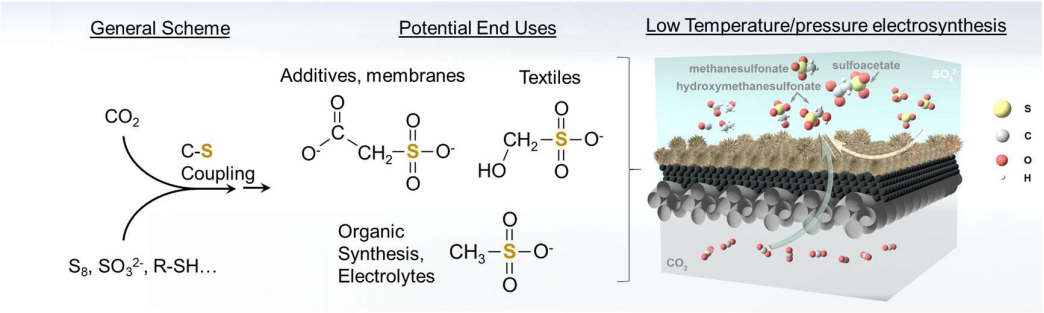

Figure 1. End-use applications of C-S bond containing products with several representative molecules and illustration of electrochemical C-S bond formation from CO_2 and SO_3^{2-} building blocks.

Result and discussion.

As a starting point, cuprous oxide catalysts were synthesized via a simple room-temperature route (Fig. S1,2).[33] A catalyst ink from these materials was loaded onto a standard gas diffusion layer and was used as the working electrode in a modified gas-diffusion half-cell configuration (Fig. S3). In this setup, CO_2 was fed through the gas phase directly to the gas/catalyst/electrolyte interface, thereby promoting CO_2 reduction by circumventing its solubility limits and enabling the use of alkaline electrolyte (1 M KOH) which suppressed the hydrogen evolution reaction (HER). 200 mM SO_3^{2-} as the sulfur source was added directly to the aqueous electrolyte. Screening of possible products in the NMR spectra revealed that HMS, SA and MS were formed as 6e^-, 8e^- and 8e^- products (Fig. 2a and S8, 9).

While enabling new reaction pathways, the presence of sulfite decreased the total current density (Fig. 2b) and favored the production of liquid products in from CO_2 reduction (Fig. 2c). Across the measured potential range, the FE for detected C-S products ranged from 4.7-9.5% (Fig. 2d) and the partial current density for each only modestly increased with more negative potentials (Fig. 2e). This weak dependence on product formation with applied potential potentially indicates that a chemical, rather than electrochemical step may be rate-determining. The production of HMS, SA and MS from CO_2 and SO_3^{2-} represents three new reaction pathways and opens up the possibility of building up a wide gamut of thiols, sulfonates, organic sulfides and more with simple electrochemical tools as an alternative to currently employed organic chemistry routes. HMS has been observed before from the nucleophilic attack of CH_2O (locally generated from CO) by SO_3^{2-} and in our case a similar coupling step may be in play.[34] SA and MS on the other hand, is tentatively thought to arise from a (near)surface SO_3^{2-}

nucleophilic attack onto a C_2 intermediate in the methane or acetate pathway. There was no HMS, SA or MS formed in control experiments that omitted CO_2, SO_3^{2-}, the Cu catalyst or an applied bias (Fig. S10). Further, using commercially purchased Cu, Cu_2O, CuO or synthesized Cu_2O with other morphologies resulted in HMS and SA formation with lower, but comparable FEs (Fig. S9, 16), indicating that the C-S bond pathway is generalizable on a variety of Cu-based materials. In contrast, Ag particles which produce CO as the main CO_2 reduction product, did not show any detectable C-S products (Fig. S17), indicating the need of the catalyst to produce and stabilize further reduced intermediates than CO. When SO_3^{2-} was omitted from the electrolyte, the main difference in the product distribution was that methane was a dominant product (Fig. S18). This may indicate that the route to C-S products shares a similar pathway to methane formation and thus intercepts intermediate before they are reduced to methane or that the presence of near-surface SO_3^{2-} alters the reaction route to minimize the methane pathway.

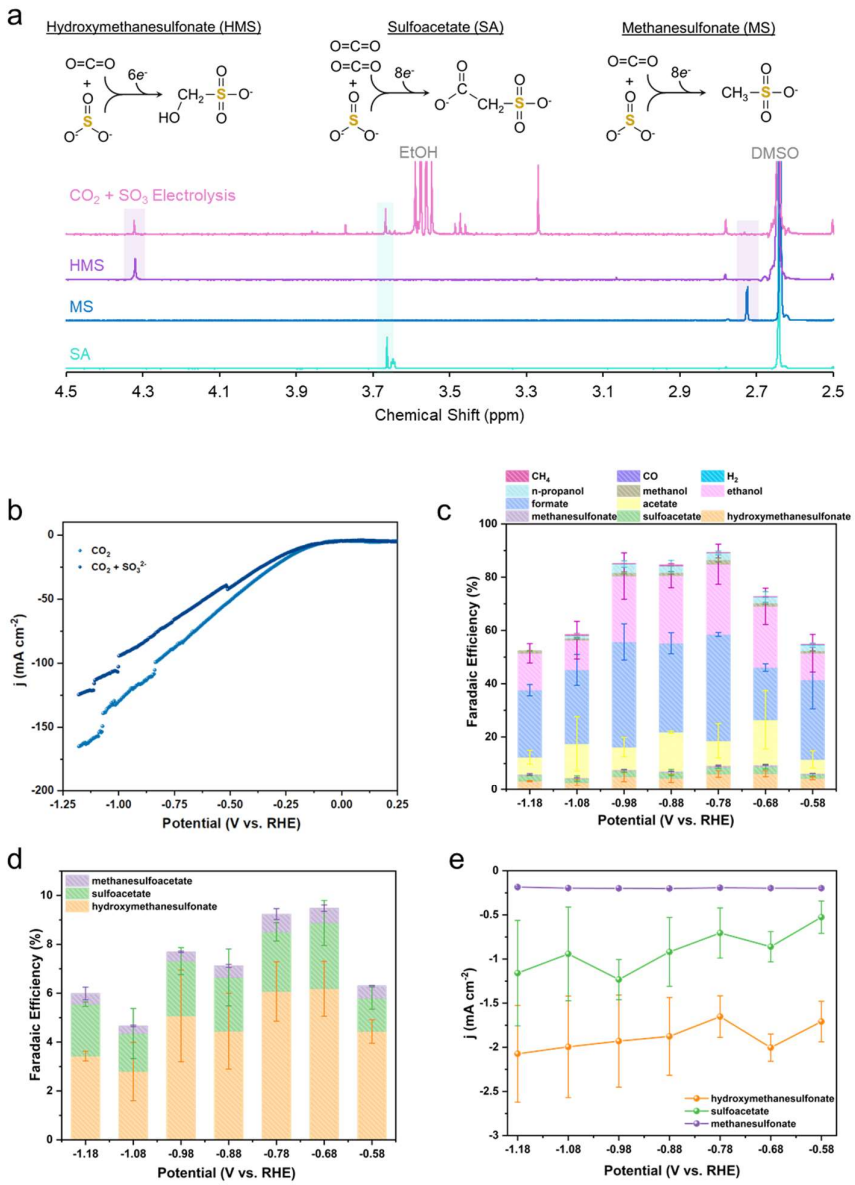

Figure 2. Identification and structure of HMS, MS and SA products constructed from CO_2 and SO_3^{2-} (a). The presence of 200 mM SO_3^{2-} decreases the overall current density (b) and pushes the selectivity towards liquid products (c). In all, C-S products are formed with up to 9.5% FE (d) with only a weak dependence of their formation rates on the applied potential (e).

We next moved to carry out a round of experimental mechanistic studies to gain an initial layer of insight into the dynamics of the electrosynthetic system. The faceted Cu_2O starting material loses its well-defined structure during electrocatalysis under reductive potentials, as evident from a comparison of transmission electron microscope (TEM) images (Fig. 3a). Translating the setup to a powder x-ray diffraction (XRD) instrument enabled us to visualize changes in crystallinity immediately after applying a reducing potential. Indeed, the Cu_2O peaks disappear within 4 minutes after shifting from open circuit conditions to -0.68V_{RHE} and only Cu peak

stemming from metallic Cu remains (Fig. 3b). This indicates that while an oxide is the starting material, the main phase of the catalyst under working conditions is indeed metallic Cu, though sub-surface oxygen or defects induced by the structural change could certainly be present and affecting the catalytic process.

Raman spectroscopy was subsequently utilized to capture the reaction intermediates on the Cu surface under equivalent reaction conditions (Fig. 3c). While the assignment of each peak is not entirely unambiguous, we base our interpretation on previously established works.[35-40]
As the potentially was systematically shifted negatively from open circuit conditions, Cu_2O bands (220 and 417-670 cm^{-1}) diminished, pointing to the transition to metallic Cu by -0.58V_{RHE}. At the same time, the Cu-CO band (369 cm^{-1}) appeared starting at -0.58V_{RHE}. Similarly, weak features potentially stemming from $*CO_{bridge}$ (1850-1900 cm^{-1}, 0.42 to -0.18 V_{RHE}) were noted (Fig. S26). In addition to CO, $*CO_2^-$ (700 cm^{-1}), SO_3^{2-} (983 cm^{-1}), HCO_3^- (1022 cm^{-1}) and CO_3^{2-} (1069 cm^{-1}) were identified as (near)surface species. These bands, with the exception of SO_3^{2-}, were similarly detected during electrolysis with CO_2 only. Finally, a set of bands at 700, 1331-1371, and 1580-1620 cm^{-1} arose under reductive potentials. While there is debate as to their exact identity, previous works have attributed them to $*COO^-$ or *COOH species and this is our tentative assignment (Fig. S26).[35,36,41,42]

In all, the main takeaways from the above experiments were that most oxide-like features disappeared from the catalyst under operating conditions, SO_3^{2-} was continually present as a (near)surface species, and CO and CO_2^- were the primary reaction intermediates on the Cu surface. Thus, CO is a likely serving principal intermediate in the reaction pathways towards higher order products. Given that the measured quantities of CO were very low, it is likely that all of the detected *CO reacted further on the catalyst surface via hydrogenation or C-C coupling. Hydrogenation would occur en route to CH_4 production while a combination of C-C coupling and hydrogenation would terminate in the observed ethanol and acetate in our system. Because the CH_4 is the primary product that is suppressed in the presence of SO_3^{2-}, it would be reasonable to assume that a partially hydrogenated *CO (e.g. *CHO, CH_2O…) in the CH_4 pathway may be the main species coupling with SO_3^{2-} en route to HMS formation. This is also consistent with the fact that C-H bands around 2800-2900 cm^{-1} are seen under C-S bond forming conditions, even as CH_4 production is suppressed (though other C-H containing products like ethanol and acetate are still produced). The Raman and XRD experiments further point to Cu as the main phase during catalysis rather than oxide or sulfide phases of Cu that were not detected within the limits of our experimental sensitivity.

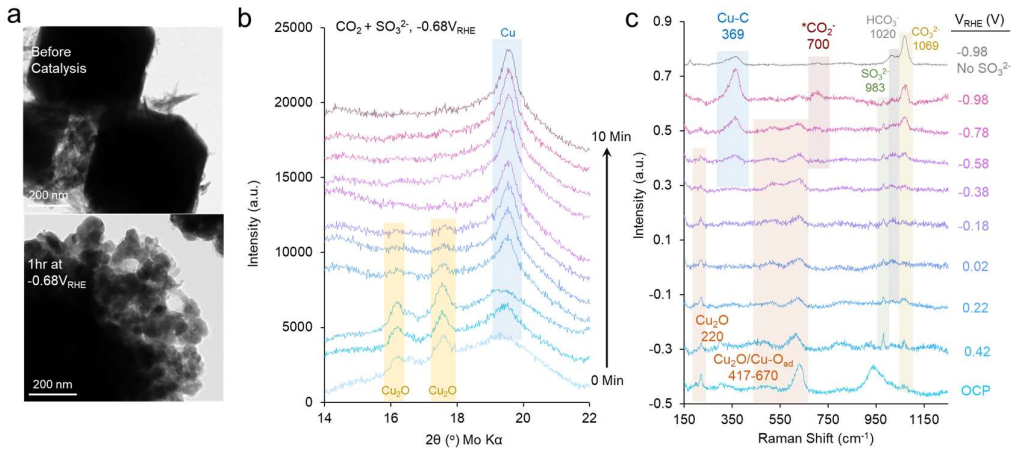

Figure 3. TEM imaging illustrates morphological changes during the catalytic cycle (a) while the changes in crystallinity are probed during the reaction with *operando* XRD measurements (b). Similarly, *operando* Raman experiments capture surface-bound intermediates en route to CO_2 and SO_3^{2-} coupling.

A complementary investigation into the mechanism for heterogeneous C-S bond formation was performed with density functional theory (DFT) computations using the results from electrocatalytic and spectroscopic experiments as a starting point. Here, three slab structures for copper (100), (110) and (111) were constructed as the model catalyst to simulate the reaction pathway. Further computational details are given in the SI and elsewhere.[43] Based on the observations in figures 2 and 3, CO was used as a starting intermediate as it is one featured in the CO_2 reduction pathway to higher order products.

To compute energy differences of elementary proton coupled electron transfer (PCET) steps, the computational hydrogen electrode (CHE) model[44] was used. Since an explicit negative charge(s) was added to the simulation for SO_3^{2-} and HSO_3^-, to calculate the energy difference of the adsorption step and coupling step, the following equations were used, respectively:

$$SO_3^{2-} + * \rightarrow {}^*SO_3 + 2e^-;\ \Delta E_{ads} = E_{{}^*SO_3} + 2eV - E_{SO_3^{2-}} - E_* \quad \text{(Rx1)}$$

$$SO_3^{2-} + {}^*CO \rightarrow {}^*SO_3CO + 2e^-;\ \Delta E_{coupling} = E_{{}^*SO_3CO} + 2eV - E_{SO_3^{2-}} - E_{{}^*CO} \quad \text{(Rx2)}$$

$${}^*SO_3 + {}^*CO \rightarrow {}^*SO_3CO;\ \Delta E_{coupling} = E_{{}^*SO_3CO} - E_{{}^*SO_3} - E_{{}^*CO} \quad \text{(Rx3)}$$

$$HSO_3^- + * \rightarrow {}^*HSO_3 + e^-;\ \Delta E_{ads} = E_{{}^*HSO_3} + eV - E_{HSO_3^-} - E_* \quad \text{(Rx4)}$$

$$HSO_3^- + {}^*CO \rightarrow {}^* HSO_3CO + e^-;\ \Delta E_{coupling} = E_{HSO_3CO} + eV - E_{HSO_3^-} - E_{{}^*CO} \quad \text{(Rx5)}$$

$${}^*HSO_3 + {}^*CO \rightarrow {}^* HSO_3CO\ ;\ \Delta E_{coupling} = E_{HSO_3CO} - E_{{}^*HSO_3} - E_{{}^*CO} \quad \text{(Rx6)}$$

To compute the energy differences for multiple reaction pathways, the basic CORR mechanisms are considered:

$$CO \longrightarrow {}^*CO \longrightarrow {}^*COH \longrightarrow {}^*C \longrightarrow {}^*CH \longrightarrow {}^*CH_2 \longrightarrow {}^*CH_3 \longrightarrow CH_4 \quad \text{(Rx7)}$$

$$CO \longrightarrow {}^*CO \longrightarrow {}^*CHO \longrightarrow {}^*CHOH\ , {}^*CH_2O \longrightarrow {}^*CH_2OH \longrightarrow CH_3OH \quad \text{(Rx8)}$$

In both pathways, except the first adsorption step the rests are PCET steps. The intermediates investigated that can couple with SO_3^{2-} or HSO_3^- are CO, COH, CHO, CHOH, CH_2O and CH_2OH. In Rx7, the intermediates following COH were not considered since formation of COH is unfavourable at 0.6 eV on Cu (100), as shown in Fig. 4. However, COH coupling with SO_3^{2-} was still considered since COH is believed to be an intermediate to methane production. For Rx8, CHO, CHOH, CH_2O and CH_2OH were coupled with SO_3^{2-} to create the C-S bond.
The final product considered in DFT calculations was HMS as seen in Fig. 2 as it is the primary C-S product in the electrolysis experiments. In solution, SO_3^{2-} or HSO_3^- can exist depending on the pH of the electrolyte. Thus, both compounds are tested for the nucleophilic attack. Furthermore, at any point during protonation, one of the oxygens attached to the sulfur can be protonated to yield -RSO_2OH. All of the aforementioned pathways are considered and this is illustrated in Fig. S27, 28.

Two mechanisms are investigated for the C-S coupling step: (*i*) a nucleophilic attack of either SO_3^{2-} (Rx2) or HSO_3^- (Rx4) on the carbon of an adsorbed intermediate; and (*ii*) surface coupling of an adsorbed $^*SO_3$ (Rx1 and Rx3) or $^*HSO_3$ (Rx4 and Rx6) with the carbon of an adsorbed intermediate.
Adsorption energy calculations of S species on all three copper facets (Table S2) reveal that: (*i*) SO_3^{2-} is adsorbed more favourably than HSO_3^-. This is mostly because SO_3^{2-}species has 2 negative charges and is relatively smaller than HSO_3^-, making it easier to bond with copper atoms (Fig. 4); (*ii*) Both S species are adsorbed more strongly on the (110) facet, followed by (100) then (111) facets, as seen on Table S2. Accordingly, the rest of the simulations to calculate the reaction energy diagram are performed only on (110) and (100) facets.
The (110) facet might perform the best as it interacts more strongly with S species compared to the other two surfaces. However, according to the Sabatier principle, the middle adsorption by (100) facet could render it the best performing as the adsorption is neither too week (not able to hold the species on the surface for enough time to react with other reaction intermediates) nor too strong (to avoid further interactions with other reaction intermediates). The reaction energy diagram is shown for the (100) facet on Fig. 5, and that for the (110) facet is demonstrated on Fig. S29.

The optimized energies for all the structures are provided in Table S3, 4. Through these DFT computations we seek: (*i*) to understand which reaction intermediates are involved in the C-S coupling step; (ii) to calculate the reaction energy barrier of the C-S coupling step; and (*iii*) to specify the best performing facet for the C-S bond formation.

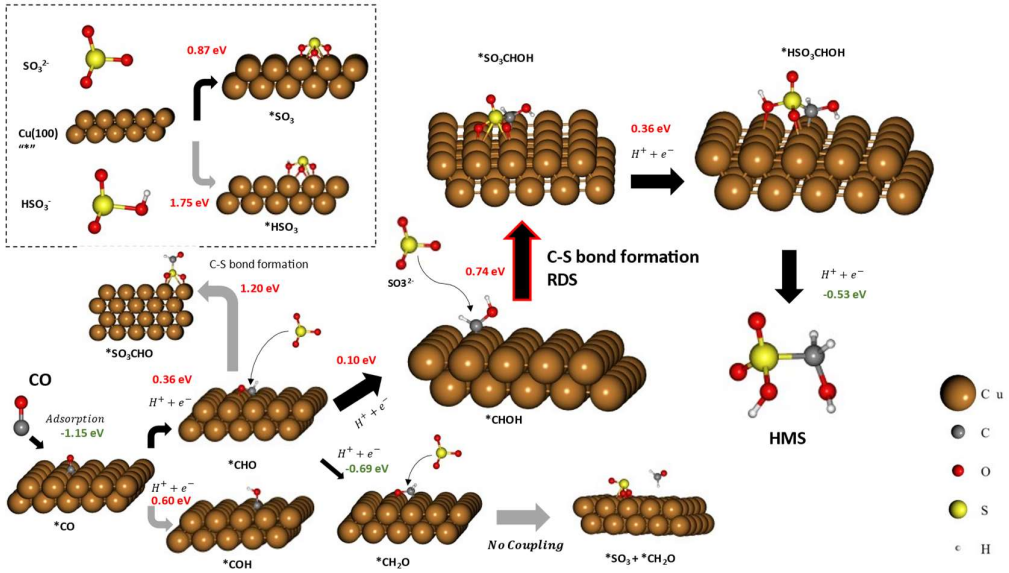

Figure 4. Reaction pathway from CO to HMS. Red numbers are positive energy barriers (uphill) while green numbers are negative (downhill).

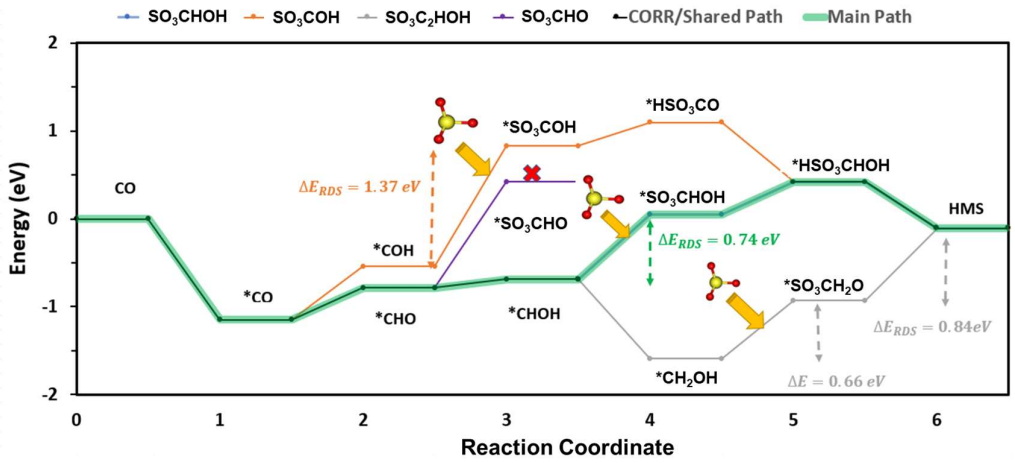

Figure 5. Energy diagram on Cu (100). The blue curve is for C-S coupling with CHOH. The orange curve is for HSO_3COH. The grey curve is for SO_3CH_2OH. The black curve on the left is the shared CORR path while the black curve on the right represents intersecting paths. The green highlighted curve shows the most favourable path to HMS.

The optimal path is shown with thick black arrows on Fig. 4. The energy diagram comparing different C-S coupling steps is shown on Fig. 5. Coupling through SO_3^{2-} is more favourable than HSO_3^-, regardless of which intermediates are involved in the C-S coupling step and no matter what the copper surface is. Furthermore, due to the high adsorption energy of $^*SO_3$ on (100), surface coupling is deemed less likely than the nucleophilic attack of the species from the electrolyte.

The optimal coupling step is found to be through *CHOH. The energy barrier of the C-S coupling step is 0.74 eV and is the rate determining step (RDS). Coupling through *COH has a large energy barrier of 1.37 eV. Surprisingly, coupling through $*CH_2OH$ has an energy barrier of 0.66 eV, which is lower than *CHOH coupling. However, protonating the sulfur of SO_3CH_2OH has a barrier of 0.82 eV, making this path unfavourable.

Comparing the energy barrier of the RDS to typical RDS's of CO_2RR, it is reasonable to observe that the maximal FE obtained in this study is ~10% since most thermodynamic energy barrier for the CO_2RR are lower than 0.74 eV. Lowering the energy barrier of the *CHOH coupling step is key to further increasing the FE in future studies.

The same methodology and calculations are applied to the (110) facet since it appears to have the lowest $^*SO_3$ adsorption energy. In other words, the (110) facet has the strongest affinity for $^*SO_3$, making it an interesting catalyst. Figure S30 shows the energy diagram of the most favourable path on both (100) and (110). The most promising coupling path on (110) appears to be consistent with *CHOH coupling being the most favourable again. The coupling energy barrier, however, is only at 0.11 eV. The largest subsequent protonation energy barrier is the protonation of sulfur in SO_3CHOH to HSO_3CHOH, at 0.29 eV as can be seen in Fig. S28, 29. Thus, the RDS remains *CO hydrogenation to *CHO, a typical RDS for the CO_2RR. The DFT results show that (110) should be superior to (100) when it comes to C-S bond formation as seen in Figure S30 however our experiments do not show that. This could be due to changes in size, surface reconstruction and other unaccounted-for effects. We encourage future studies to explore the Cu (110) facet further.

As a final step, we sought to expand the scope in terms of potential C-S coupling reactions. While the partial current densities for C-S products was rather modest when using CO_2 as the reactant, amounting to less than 5 mA/cm^2, we reasoned that potentially more active C-precursors that can be produced from CO_2 reduction would lead to enhanced rates (Fig. 6a). To this end, we maintained identical reaction conditions (-1.18V_{RHE}, 200 mM SO_3^{2-} in 1 M KOH) and substituted 200 mM of CH_3OH, $HCOO^-$, CH_2O or CH_3COO^- in place of CO_2. Indeed, we was that the formation of SA was greatly increased by up to 2 orders of magnitude for CH_3OH and by 30X for $HCOO^-$ (Fig. 6b). Note, no products were observed if SO_3^{2-} and the C-reactants were simply mixed in the electrolyte (Fig. S30). The equilibration with methanediol in alkaline media likely prevented formaldehyde from directly coupling with SO_3^{2-} through non-electrochemical steps. We chose to use formation rate as a metric of comparison as the precise mechanism and electron transfer steps are not yet unambiguous. This set of results indicates that a variety of partially reduced CO_2 products species may act as effective building blocks for C-C and C-S bond formation. Strategies for C-S product synthesis with increased rates could then entail the use of flow reactors utilize a CO_2 activation catalyst (e.g. Sn or Bi – based materials selective for $HCOO^-$) and a secondary C-S coupling catalyst (Cu in this work but

other materials may yet be better). Interestingly, HMS was not observed in these experiments, and this can be rationalized as the reactants used did not feature the key intermediates of *COH or *CHOH as calculated above.

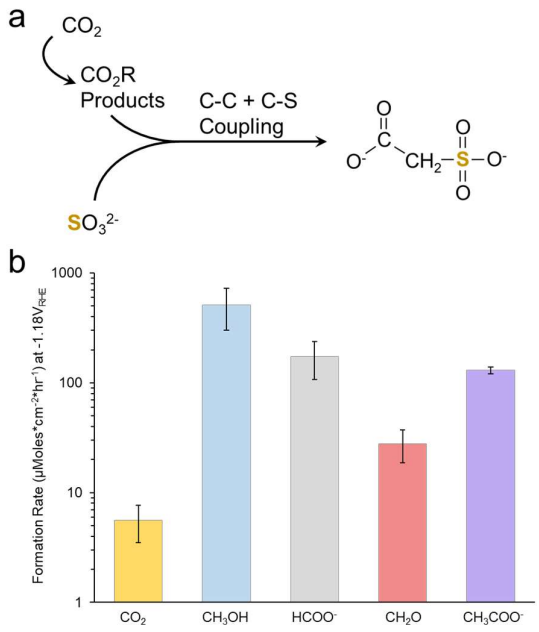

Figure 6. Scheme of using partially reduced CO_2 products as activated reagents for C-S bond formation (a). The formation rate of SA at -1.18V_{RHE} is significantly enhanced when substituting 200 mM of C-reactant in place of CO_2 (b).

Concluding Remarks

In all, this work develops the first C-S coupling pathway via heterogeneous electrocatalysis using CO_2 as a building block. Using Cu-based catalysts as a model system, we illustrate how CO_2 is reduced to surface-bound electrophilic intermediates like *CHOH, which are then subject to nucleophilic attack by near-surface SO_3^{2-} species, yielding three distinct C-S bond containing species. The expansion of scope of CO_2 reduction to include products with C-S bonds is set to grant electrocatalytic technologies access to not only fuels and commodity chemicals, but also to important sets of fine/specialty chemicals and widen the impact of this growing domain.

Acknowledgements:
N.K. and J. L. acknowledge NSERC for its Discovery Grant RGPIN-2019-05927. A.S. acknowledges NSERC for its Discovery Grant RGPIN-2020-04960 and Canada Research Chair (950-23288). Computations in this research were enabled in part by support provided by Calcul Quebec and Compute Canada.

Declaration of Interests:
The authors declare no competing interests

Data Availability Statement:
All data will be deposited in *Papyrus*, a publicly accessible repository.

References:

1 Lagadec, M. F. & Grimaud, A. Water electrolysers with closed and open electrochemical systems. *Nat. Mater.* **19**, 1140-1150 (2020).

2 Ross, M. B. *et al.* Designing materials for electrochemical carbon dioxide recycling. *Nat. Catal.* **2**, 648-658 (2019).

3 Masel, R. I. *et al.* An industrial perspective on catalysts for low-temperature CO2 electrolysis. *Nat. Nanotechnol.* **16**, 118-128 (2021).

4 Zhang, Y., Li, J. & Kornienko, N. Strategies for heterogeneous small-molecule electrosynthesis. *Cell Rep. Phys. Sci.* **2**, 100682 (2021).

5 Perry, S. C. *et al.* Electrochemical synthesis of hydrogen peroxide from water and oxygen. *Nat. Rev. Chem.* **3**, 442-458 (2019).

6 Suryanto, B. H. R. *et al.* Challenges and prospects in the catalysis of electroreduction of nitrogen to ammonia. *Nat. Catal.* **2**, 290-296 (2019).

7 Li, J., Zhang, Y., Kuruvinashetti, K. & Kornienko, N. Construction of C–N bonds from small-molecule precursors through heterogeneous electrocatalysis. *Nat. Rev. Chem.* **6**, 303-319 (2022).

8 Fontecave, M., Ollagnier-de-Choudens, S. & Mulliez, E. Biological Radical Sulfur Insertion Reactions. *Chem. Rev.* **103**, 2149-2166 (2003).

9 Mansy, S. S. & Cowan, J. A. Iron−Sulfur Cluster Biosynthesis: Toward an Understanding of Cellular Machinery and Molecular Mechanism. *Acc. Chem. Res.* **37**, 719-725 (2004).

10 Zhao, C., Rakesh, K. P., Ravidar, L., Fang, W.-Y. & Qin, H.-L. Pharmaceutical and medicinal significance of sulfur (SVI)-Containing motifs for drug discovery: A critical review. *Eur. J. Med. Chem.* **162**, 679-734 (2019).

11 Devendar, P. & Yang, G.-F. in *Sulfur Chemistry* (ed Xuefeng Jiang) 35-78 (Springer International Publishing, 2019).

12 Rosenman, A. *et al.* Review on Li-Sulfur Battery Systems: an Integral Perspective. *Adv. Energy Mater.* **5**, 1500212 (2015).

13 Barbarella, G., Melucci, M. & Sotgiu, G. The Versatile Thiophene: An Overview of Recent Research on Thiophene-Based Materials. *Adv. Mater.* **17**, 1581-1593 (2005).

14 Sakakura, A., Yamada, H. & Ishihara, K. Enantioselective Diels–Alder Reaction of α-(Acylthio)acroleins: A New Entry to Sulfur-Containing Chiral Quaternary Carbons. *Org. Lett.* **14**, 2972-2975 (2012).

15 Wu, X.-S., Chen, Y., Li, M.-B., Zhou, M.-G. & Tian, S.-K. Direct Substitution of Primary Allylic Amines with Sulfinate Salts. *J. Am. Chem. Soc.* **134**, 14694-14697 (2012).

16 Mukhopadhyay, S. & Bell, A. T. Catalyzed sulfonation of methane to methanesulfonic acid. *J. Mol. Catal. A: Chem.* **211**, 59-65 (2004).

17 Uraguchi, D., Kinoshita, N., Nakashima, D. & Ooi, T. Chiral ionic Brønsted acid–achiral Brønsted base synergistic catalysis for asymmetric sulfa-Michael addition to nitroolefins. *Chem.*

Sci. **3**, 3161-3164 (2012).

18 Savateev, A., Kurpil, B., Mishchenko, A., Zhang, G. & Antonietti, M. A "waiting" carbon nitride radical anion: a charge storage material and key intermediate in direct C–H thiolation of methylarenes using elemental sulfur as the "S"-source. *Chem. Sci.* **9**, 3584-3591 (2018).

19 Su, F. *et al.* Aerobic Oxidative Coupling of Amines by Carbon Nitride Photocatalysis with Visible Light. *Angew. Chem. Int. Ed.* **50**, 657-660 (2011).

20 Britschgi, J., Kersten, W., Waldvogel, S. R. & Schüth, F. Electrochemically Initiated Synthesis of Methanesulfonic Acid. *Angew. Chem. Int. Ed.* **61**, e202209591 (2022).

21 Li, J. & Kornienko, N. Electrochemically driven C–N bond formation from CO2 and ammonia at the triple-phase boundary. *Chem. Sci.* **13**, 3957-3964 (2022).

22 Chen, C. *et al.* Coupling N_2 and CO_2 in H_2O to synthesize urea under ambient conditions. *Nat. Chem.* **12**, 717-724 (2020).

23 Wu, Y., Jiang, Z., Lin, Z., Liang, Y. & Wang, H. Direct electrosynthesis of methylamine from carbon dioxide and nitrate. *Nat. Sustainability* **4**, 725-730 (2021).

24 Meng, N., Huang, Y., Liu, Y., Yu, Y. & Zhang, B. Electrosynthesis of urea from nitrite and CO2 over oxygen vacancy-rich ZnO porous nanosheets. *Cell Rep. Phys. Sci.* **2**, 100378 (2021).

25 Rayner-Canham, G. Isodiagonality in the periodic table. *Found. Chem.* **13**, 121-129 (2011).

26 Nitopi, S. *et al.* Progress and Perspectives of Electrochemical CO2 Reduction on Copper in Aqueous Electrolyte. *Chem. Rev.* **119**, 7610-7672 (2019).

27 Nascimento, B. *et al.* Application of cellulose sulfoacetate obtained from sugarcane bagasse as an additive in mortars. *J. App. Polym. Sci.* **124**, 510-517 (2012).

28 Seeponkai, N. & Wootthikanokkhan, J. Proton conductivity and methanol permeability of sulfonated poly(vinyl alcohol) membranes modified by using sulfoacetic acid and poly(acrylic acid). *J. App. Polym. Sci.* **105**, 838-845 (2007).

29 D. Gernon, M., Wu, M., Buszta, T. & Janney, P. Environmental benefits of methanesulfonic acid . Comparative properties and advantages. *Green Chem.* **1**, 127-140 (1999).

30 Balaji, R. & Pushpavanam, M. Methanesulphonic acid in electroplating related metal finishing industries. *Trans. IMF* **81**, 154-158 (2003).

31 Nacsa, E. D. & Lambert, T. H. Cyclopropenone Catalyzed Substitution of Alcohols with Mesylate Ion. *Org. Lett.* **15**, 38-41 (2013).

32 V. Makarov, S. Recent trends in the chemistry of sulfur-containing reducing agents. *Russ. Chem. Rev.* **70**, 885-895 (2001).

33 Ho, J.-Y. & Huang, M. H. Synthesis of Submicrometer-Sized Cu2O Crystals with Morphological Evolution from Cubic to Hexapod Structures and Their Comparative Photocatalytic Activity. *J. Phys. Chem. C* **113**, 14159-14164 (2009).

34 Boutin, E., Salamé, A., Merakeb, L., Chatterjee, T. & Robert, M. On the Existence and Role of Formaldehyde During Aqueous Electrochemical Reduction of Carbon Monoxide to Methanol by Cobalt Phthalocyanine. *Chem. Eur. J* **28**, e202200697 (2022).

35 Chernyshova Irina, V., Somasundaran, P. & Ponnurangam, S. On the origin of the elusive first intermediate of CO2 electroreduction. *Proc. Natlù Acad. Sci. U.S.A.* **115**, E9261-E9270 (2018).

36 Firet, N. J. & Smith, W. A. Probing the Reaction Mechanism of CO2 Electroreduction over Ag Films via Operando Infrared Spectroscopy. *ACS Catal.* **7**, 606-612 (2017).

37 Gunathunge, C. M. *et al.* Spectroscopic Observation of Reversible Surface Reconstruction of Copper Electrodes under CO2 Reduction. *J. Phys. Chem. C* **121**, 12337-12344 (2017).

38 Chen, X. *et al.* Controlling Speciation during CO2 Reduction on Cu-Alloy Electrodes. *ACS Catal.* **10**, 672-682 (2020).

39 Li, X. *et al.* Selective visible-light-driven photocatalytic CO2 reduction to CH4 mediated by atomically thin CuIn5S8 layers. *Nat. Energy* **4**, 690-699 (2019).

40 Zhao, Y. *et al.* Speciation of Cu Surfaces During the Electrochemical CO Reduction Reaction. *J. Am. Chem. Soc.* **142**, 9735-9743 (2020).

41 Niu, Z.-Z. *et al.* Hierarchical Copper with Inherent Hydrophobicity Mitigates Electrode Flooding for High-Rate CO2 Electroreduction to Multicarbon Products. *J. Am. Chem. Soc.* **143**, 8011-8021 (2021).

42 Pan, Z. *et al.* Intermediate Adsorption States Switch to Selectively Catalyze Electrochemical CO2 Reduction. *ACS Catal.* **10**, 3871-3880 (2020).

43 Al-Mahayni, H., Wang, X., Harvey, J.-P., Patience, G. S. & Seifitokaldani, A. Experimental methods in chemical engineering: Density functional theory. *Can. J. Chem. Eng.* **99**, 1885-1911 (2021).

44 Nørskov, J. K. *et al.* Origin of the Overpotential for Oxygen Reduction at a Fuel-Cell Cathode. *J. Phys. Chem. B* **108**, 17886-17892 (2004).

Electrochemical Formation of C-S Bonds from CO_2 and Small Molecule Sulfur Species

Junnan Li,[a,1] Hasan Al-Mahayni,[b,1] Daniel Chartrand,[a] Ali Seifitokaldani,[b*] and Nikolay Kornienko[a*]

[1]Equal contribution

[a]Department of Chemistry, Université de Montréal, 1375 Ave. Thérèse-Lavoie-Roux, Montréal, QC H2V 0B3

[b]Department of Chemical Engineering, McGill University, 3610 University Street, Montréal, H3A 0C5 Québec, Canada

[*]Correspondence to: ali.seifitokaldani@mcgill.ca and nikolay.kornienko@umontreal.ca

Materials and methods

Chemical Reagents:

Anhydrous copper chloride ($CuCl_2$, 98%), copper nano powder (Cu, 99.9%), copper (II) oxide nano powder (CuO), hydroxylamine hydrochloride ($NH_2OH{\cdot}HCl$, 99%) were purchased from Alfa Aesar. Sodium hydroxide (NaOH, 98%) and sodium sulfite ($NaSO_4$, 98%) were acquired from Sigma-Aldrich. Potassium hydroxide was obtained from Macron fine chemicals. Copper (I) oxide was purchased from thermos scientific. Sodium dodecyl sulfate (SDS, 100%) was purchased from Mallinckrodt. All chemicals were used without further purification.

Catalyst Preparation:

Cu_2O catalysts were synthesized by a simple wet chemistry method according to the reference.[1] 1 mL of 0.1M $CuCl_2$ was added into 95.5 mL deionized (DI) water, then 2mL of 1M NaOH solution was added into the above solution under stirring. After 10 s, 0.87g SDS was added into the above mixture with vigorous stirring to make the powder solve into the solution. Then 3.5 mL of 0.2M $NH_2OH{\cdot}HCl$ was injected into the above mixture and was shaken for 10 s. The mixture was centrifuged to obtain the precipitates after 12 h aging, and washed with water and ethanol three times, respectively. Finally, the precipitates were dried in a vacuum oven for 12h, and the powder was labeled as sample C. This was the primary catalyst used for electrocatalytic measurements

For sample A to H, the synthesis steps are similar to sample C, except for different volumes of DI water and $NH_2OH{\cdot}HCl$. The volume of DI water and $NH_2OH{\cdot}HCl$ for each sample were listed in Table 1.

Table 1. The volume of DI water and $NH_2OH{\cdot}HCl$ for the synthesis different Cu_2O/CuO samples:

	DI water (mL)	$NH_2OH{\cdot}HCl$ (mL)
A	95.5	1.5
B	94.5	2.5
C	93.5	3.5
D	92.5	4.5
E	91.5	5.5
F	90.5	6.5
G	87.5	9.5
H	91	7.5 (adjust to pH 7)

Characterizations:

Ex-situ X-ray diffraction (XRD) patterns were collected with a Malvern PanAlytical Empyrean 3 diffractometer with a Cu Kα radiation source (λ = 1.5418 Å) and a PIXcel^{3D} detector in 1D mode operated in Bragg Brentano (θ-θ) geometry, using iCore and dCore optics with automatic slits set at 10 mm irradiated length and a collection time of 1h. In contrast, a Mo-source was used for *in operando* measurements due to its higher penetration, high intensity and compressed pattern which allow to measure all peak of interests in a static configuration. They were collected on a Malvern PanAlytical Empyrean 3 diffractometer with a Mo Kα radiation source (λ = 0.7093 Å) with focusing

mirror optics and a GaliPIX^{3D} detector in static 1D mode with 30 s integration time, and an omega angle of 12,5°. Scanning electron microscope characterization was conducted on FEI Quanta 450 Environmental Scanning Electron Microscope (FE-ESEM). Transmission electron microscopy (TEM) images were obtained with a JEOL JEM-2100F FEG-TEM, operating on 200 kV.

Electrochemical measurements and product qualification:

Electrochemical measurements were performed by Bio-Logic SP-200 Potentiostat (BioLogic Science Instruments, France) in a gas diffusion electrode (GDE) – based reaction cell with a three-electrode framework. Carbon rod and Ag/AgCl were utilized as the counter electrode and reference electrode, respectively. All potentials measured in this work were converted to RHE by the following equation:

E (vs RHE) = E (vs Ag/AgCl) + 0.197 + (0.0591 x pH)

The working electrode was prepared as below: 10 mg catalyst was added into the mixture of 100 μL DI water and 300 μL ethanol. After 10 mins ultrasonication, 100 μL homogeneous catalyst ink was dropped onto the carbon cloth (GDL-CT (W1S1009, Fuel Cells Etc.) and dried in air for 1h. 1M KOH with different concentrations of $NaSO_4$ was used as the electrolyte. Linear sweep voltammetry was measured in the range of 0 ~ 1.18 V (vs. RHE), with a sweep rate of 5 mV s^{-1}. Potentiostatic electrolysis was performed at room temperature and pressure, with a steady CO_2 gas flow which is 10 mL min^{-1}. The GDE cell was sealed and connected with gas chromatography (GC, SRI 8610C) to qualify the gas products in flow mode. A thermal conductivity detector (TCD) was used for analyzing H_2, and flame ionization detector (FID) was used for quantifying CO and CH_4. After 30 mins reaction, the electrolyte was collected and analyzed by ^{1}H nuclear magnetic resonance (NMR, Bruker AVII 500) and confirmed by ^{13}C NMR (NMR, Bruker AVANCE II 700). 400 μL liquid product was mixed with 400 μL D_2O, with dimethyl sulfoxide (DMSO) as an internal standard. The yield of gas and liquid products were calculated based on the calibration curves of the standard samples. The Faradaic efficiency (FE) was calculated by the following formula: $\varepsilon_{FE} = \frac{\alpha n F}{Q}$

where α is electron transfer number, n is the moles of products, F is the Faraday constant (96485 C mol^{-1}), Q is all the charge passed during the reaction.

In-situ Raman spectroscopy

In-situ Raman spectra were collected on Renishaw Invia system with a 633 nm laser. The output powder is 5 mW. Before each experiment, Raman frequency calibration was conducted by measuring a Si wafer (520 nm). A laser line focus module was utilized to obtain spectra by spreading out the laser intensity with approximately 20x lower signal intensity per area. The accumulation time per spectrum was set to 1s and the total signal acquisition time is 60s (average of 60 spectra). An immersion objective (numerical aperture of 0.8) was used to decrease the distance between the laser and the surface of the electrode to a obtain better Raman signal. The spectra were collected under different potential, range from open circuit potential to -0.98V vs. RHE, with the step of -0.2V.

The reaction cell is similar with electrochemical measurement. The same three-electrode configuration was used for the *operando* Raman measurement; working electrode, counter and reference electrode are the identical. KOH was used as electrolyte, with or without the addition of

sulfite. CO_2 or N_2 was fed into the reactor, with flow rate of 10 mL min^{-1}.

DFT parameters and computational details

Here, three slab structures for copper (100), (110) and (111) were constructed using Atomic Simulation Environment (ASE) [33] and all consisted of $5 \times 5 \times 4$ structures, or 4 layers of 25 atoms. The bottom two layers were fixed to simulate the bulk and the top two layers were free to relax to resemble the surface. 15 Å of vacuum is added in the z direction (perpendicular to the surface) to avoid interaction between periodic images. The Monkhorst-Pack scheme was used for K-points of $4 \times 4 \times 1$. The energy cut-off and the relative cut-off used were 550 and 50 Rydberg, respectively. The force convergence was taken to be 3×10^{-4} $Bohr^{-1}$ Hartree. The exchange correlation functional of Perdew, Burke, and Ernzerhof (PBE) was used.[34] All these parameters were chosen after running convergence and sensitivity tests. DFT calculations are all performed using CP2K code [35] and further computational details are given elsewhere.[36] CO was used as a starting intermediate as it one featured in the CO_2 reduction pathway to higher order products.

To compute energy differences of elementary proton coupled electron transfer (PCET) steps, the computational hydrogen electrode (CHE) model [37] was used. In this model we assume hydrogen gas is at equilibrium with proton and electron and the corresponding potential is 0 V vs. RHE, thus the energy of proton coupled with electron is estimated by half of the energy of hydrogen gas:

$$H^+ + e^- \leftrightarrow \frac{H_{2(g)}}{2} \quad \text{(Eq. 1)}$$

$$E_{H^+ + e^-} = \frac{E_{H_2(g)}}{2}, \text{ @ pH=0 and 1 atm} \quad \text{(Eq. 2)}$$

Both SO_3^{2-} and HSO_3^- are adsorbed on the Cu (111), (110) and (100). The adsorption energies are used as predictors for the affinity of the surfaces to both species. The adsorption energies are on Table S2.

Table S3 and Table S4 are the optimized energy of the copper surfaces and absorbed intermediates, respectively.

Supplementary Figures

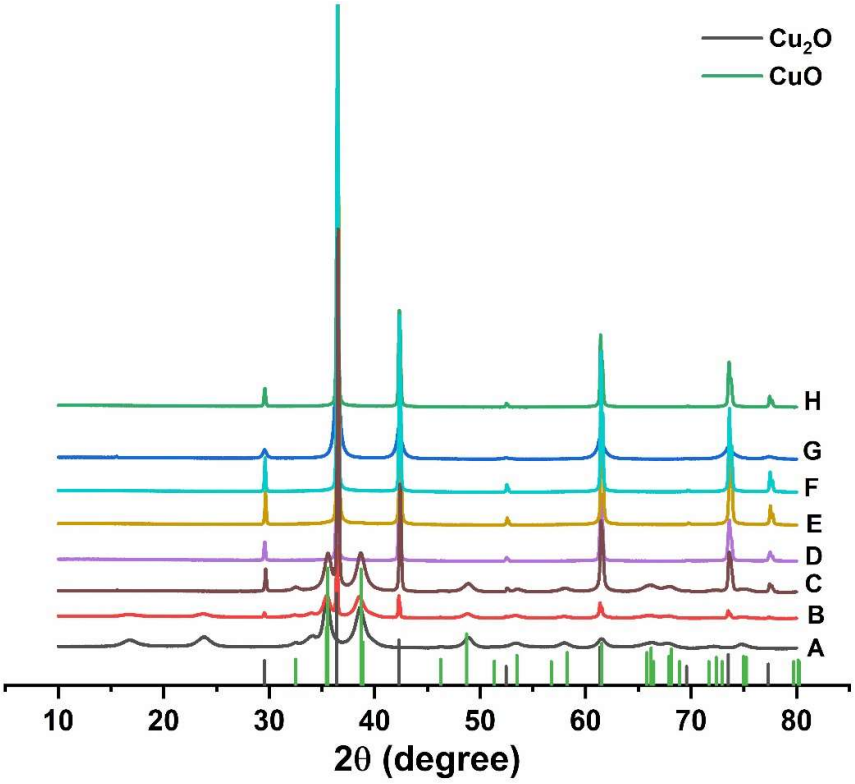

Figure S1. XRD patterns of the catalysts en route to their synthesis. Among them, sample A is CuO, sample B and C are the mixtures of CuO and Cu_2O. Sample D to H are Cu_2O.

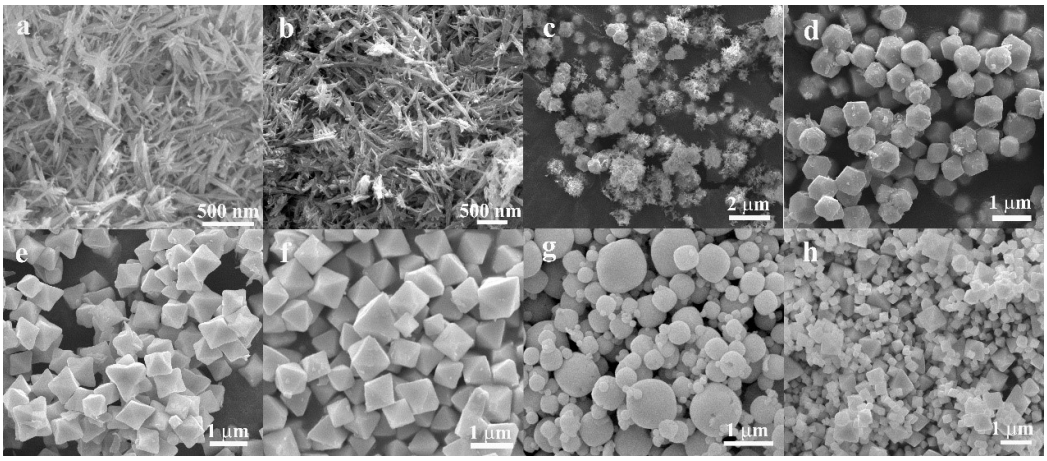

Figure S2. Typical SEM images of different catalysts from samples A to H. (a) nanowire, length is around 400 nm; (b) nanowire; (c) sample C, the aggregation of nanowire to form shaped nanoparticles, with a small amount of incompletely grown truncated octahedron crystals; (d) truncated octahedra, the size is around 600 nm; (e) short hexapods, with small amount of octahedra, ~1 μm; (f) octahedra with uniform size; (g) sphere, size distributed from 100 nm to 1 μm; (h) octahedra with a large size distribution from 200 nm to 700 nm.

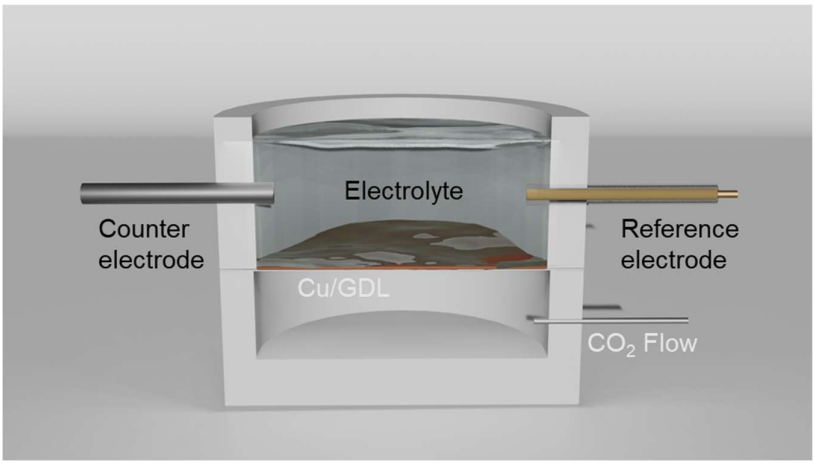

Figure S3. Gas diffusion half-cell with minimal electrolyte volume used for electrochemical screening experiments. Isolating the counter electrode with an anion-exchange membrane did not lead to a measurable difference in C-S product formation in control experiments.

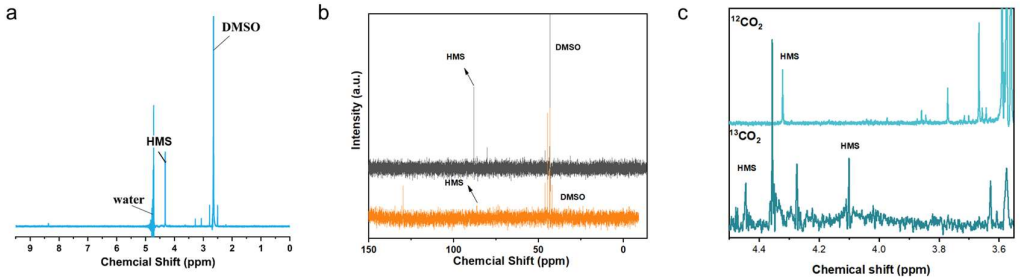

Figure S4. HNMR spectrum of hydroxymethanesulfonate (HMS) standard sample (Concentration: 20 mM in 1 M KOH) (a) and comparison of ^{13}C NMR spectra of the post-electrolysis solution (orange) and HMS standard (gray) (b). HMS also features two distinct peaks when carrying out CO_2 reduction with $^{13}CO_2$ as opposed to a single peak at 4.3 ppm when $^{12}CO_2$ is used as the carbon reagent (c).

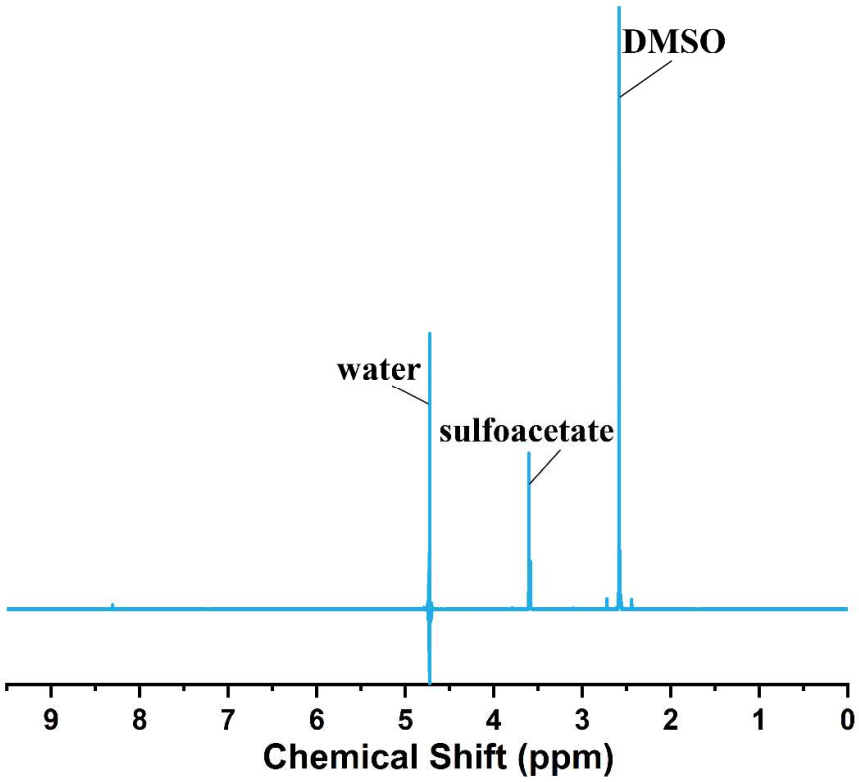

Figure S5. NMR spectrum of sulfoacetate standard sample (Concentration: 20 mM in 1 M KOH).

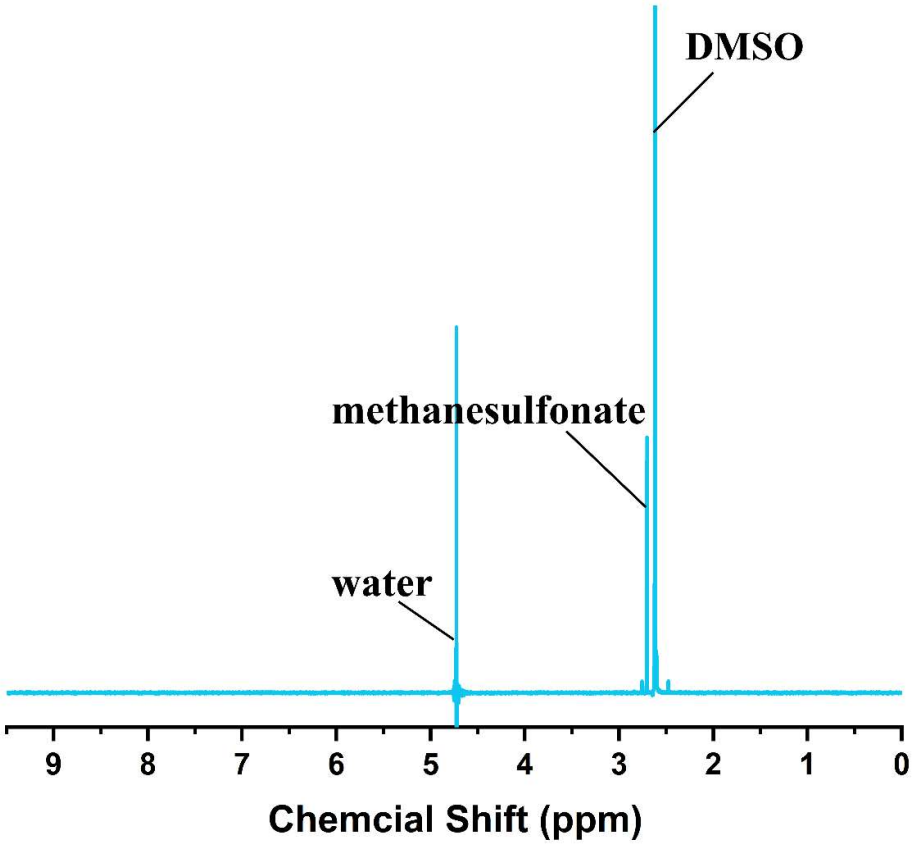

Figure S6. NMR spectrum of methanesulfonate standard sample (20 mM in 1 M KOH).

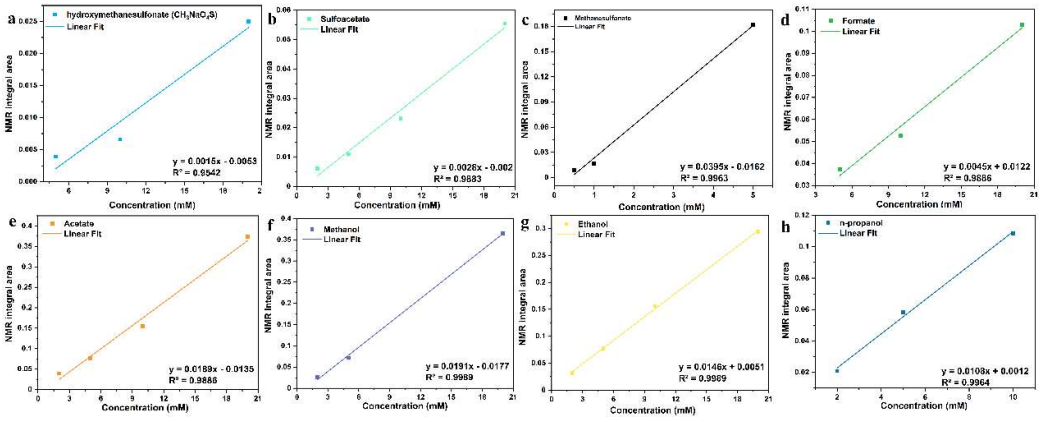

Figure S7. NMR calibration curves. (a) hydroxymethanesulfonate (HMS); (b) sulfoacetate (SA); (c) methanesulfonate (d); formate (e) acetate; (f) methanol; (g) ethanol; (h) n-propanol.

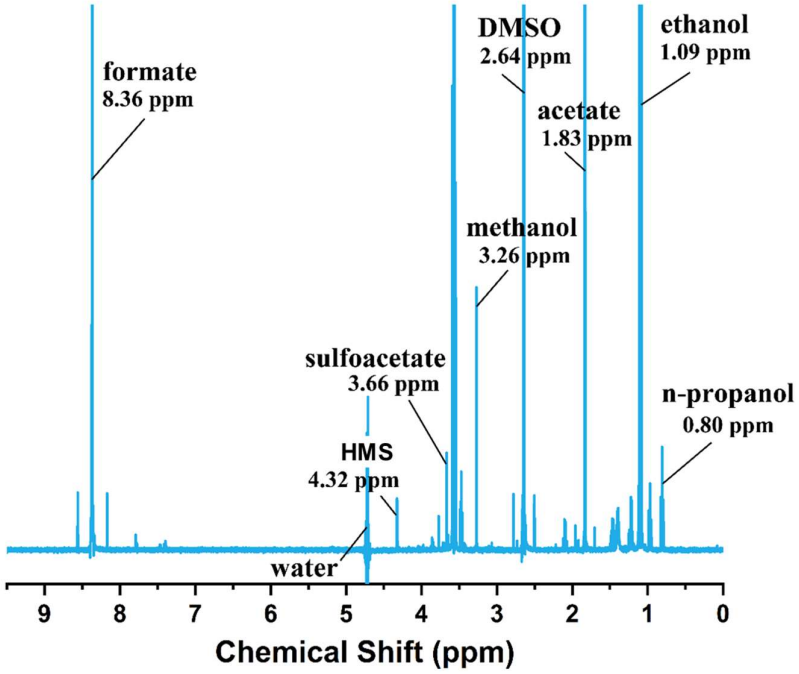

Figure S8. NMR spectrum of the liquid after potentiostatic electrolysis. Sample C was chosen as electrocatalyst with 1 M KOH, 0.2 M $NaSO_4$ as electrolyte. CO_2 gas flow rate is 10 mL min^{-1}, the applied potential is -0.78V (vs. RHE). DMSO was used as the internal standard (2.64 ppm). Hydroxymethanesulfonate (4.32 ppm, HMS) and sulfoacetate (3.66 ppm) are the product with C-S bond, the liquid products also contain formate (8.36 ppm), ethanol (1.09 ppm), acetate (1.83 ppm), methanol (3.26 ppm), and n-propanol (0.80 ppm).

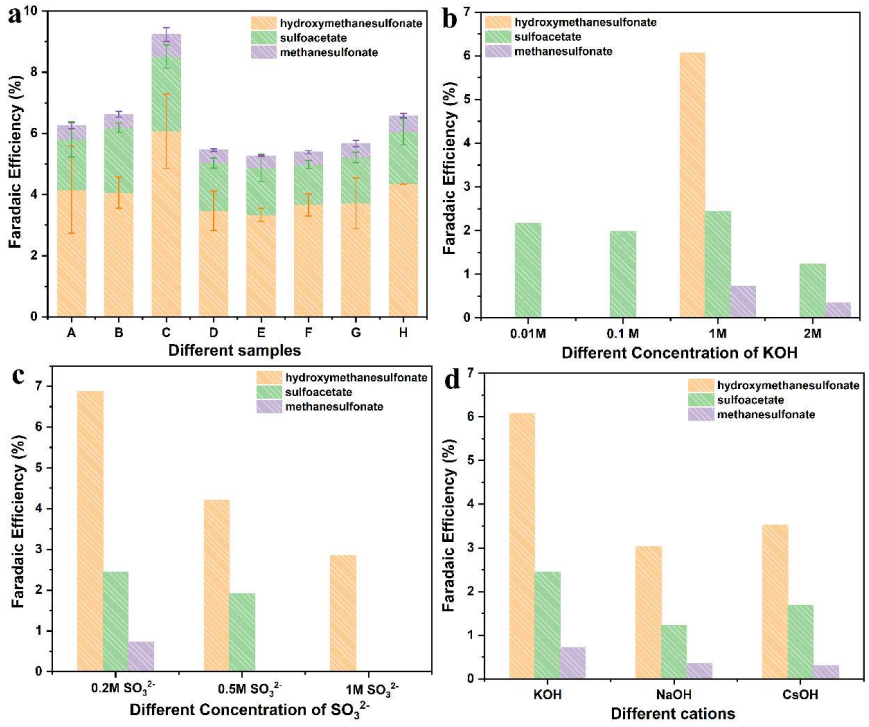

Figure S9. Optimization of reaction conditions for HMS formation. (a) FE with different Cu samples in 1 M KOH, 0.2 M Na_2SO_3, at -0.78 V. Sample C shows the highest FE among these eight catalysts. (b) Catalytic performance of sample C in different electrolytes. All the concentration is 1M. (c) Production of HMS in different concentrations of Na_2SO_3. Sample C shows the highest FE for HMS in 1M KOH, 0.2 M Na_2SO_3. Different amounts of KOH (0.1 M, 2 M) are also used as the electrolyte to adjust the pH, but no signal of HMS was observed in NMR spectrum. Loading amount has also been changed (10 mg, 15 mg, 25 mg), C-S bonds product was obtained only when the amount of sample C is 25 mg, which is 2.39, it's similar to 10 mg, thus in the following electrochemical experiment 10 mg sample C, 1 M KOH, 0.2 M $Na_2SO_3$was chosen as the reaction condition.

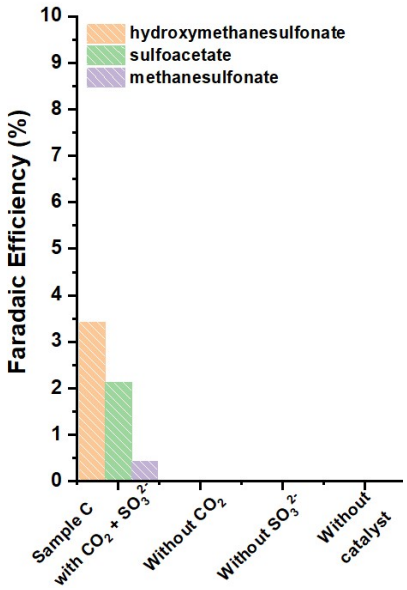

S10. Control experiments omitting key aspects of the electrocatalytic system in otherwise identical conditions (1 M KOH electrolyte, -1.18 V vs. RHE)

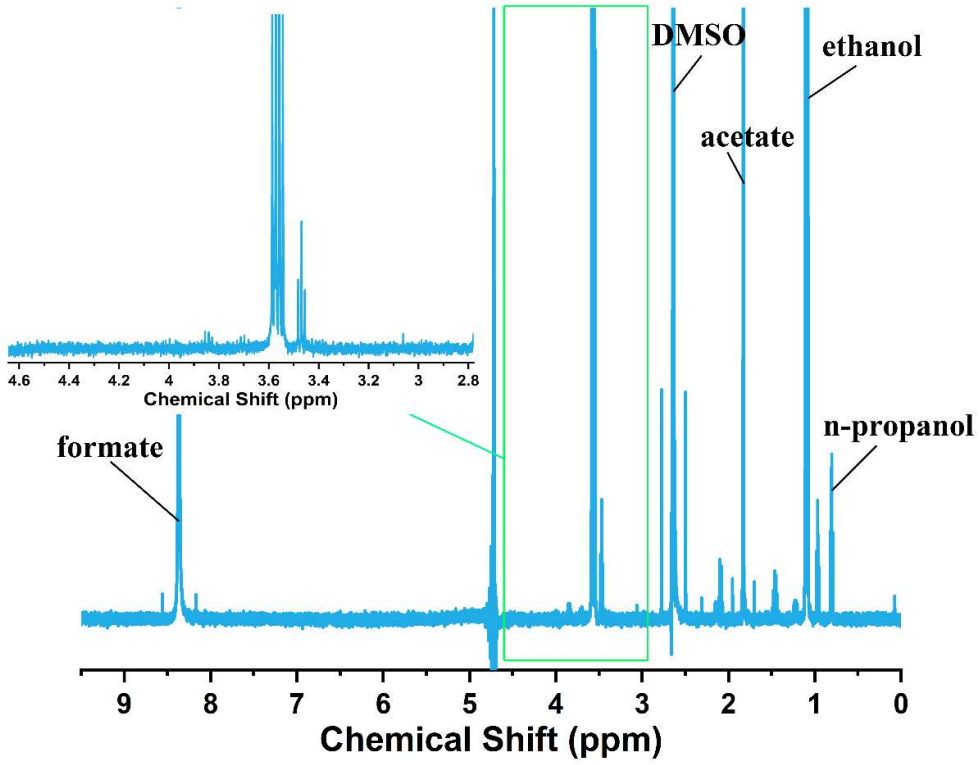

Figure S11. NMR spectrum of a control experiment performed without sulfite. Potentiostatic electrolysis was conducted with sample C in KOH + CO_2 flow under -0.78V. No HMS or sulfoacetate or MS were observed in the NMR spectrum, which proves that SO_3^{2-} is the sulfur source. Formate, acetate, ethanol, and n-propanol were observed as the final liquid products.

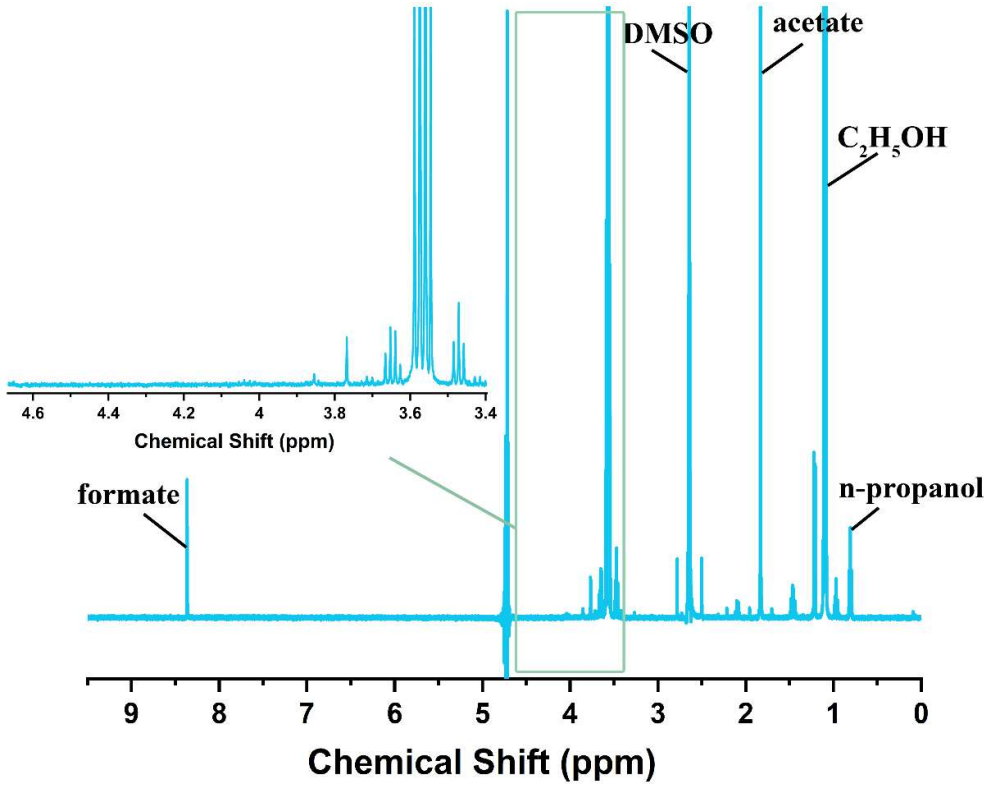

Figure S11. NMR spectrum of a control experiment without sample C. The carbon cloth was used as the electrode, 1 M KOH, 0.2 M sulfite was used as electrolyte. The electrolysis was conducted under -0.68V, with continuous CO_2 flow. No product with C-S bonds was observed. Formate, acetate, ethanol, n-propanol and methanol were observed after the reaction.

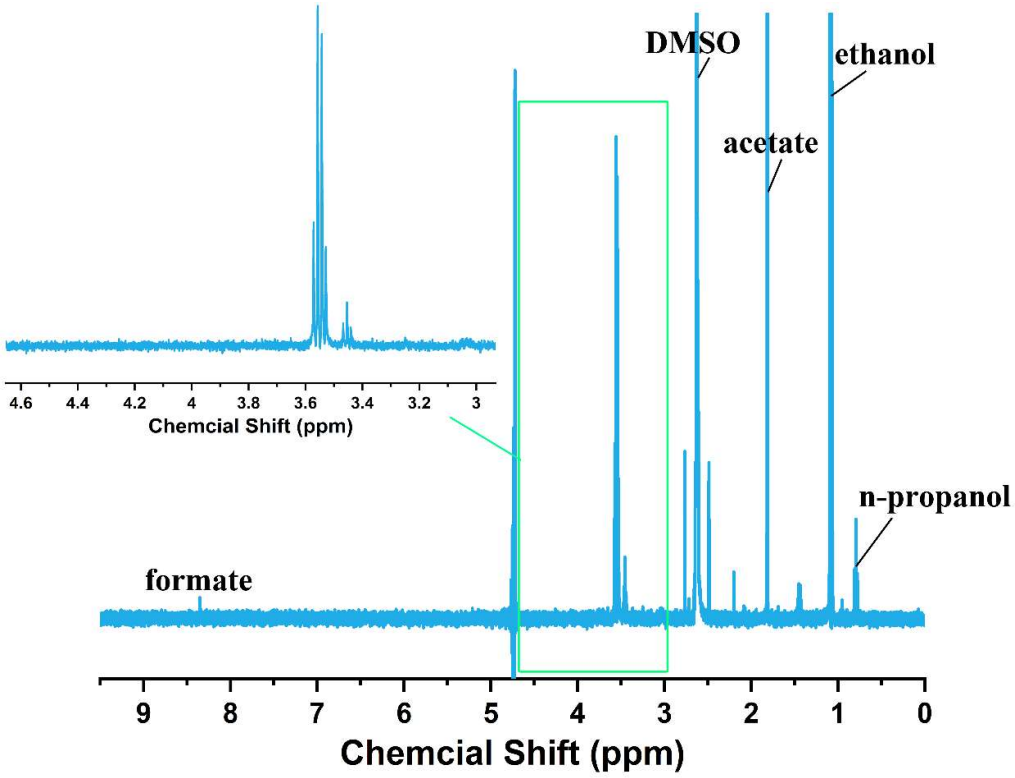

Figure S12. NMR spectrum of control experiment without CO_2. Sample C was used as the electrocatalyst, 1M KOH + 0.2 M Na_2SO_3 was used as the electrolyte, a stable, continuous N_2 gas flow was used instead of CO_2. The flow rate is 10 mL min^{-1}. No C-S bond compounds are obtained after electrolysis, formate, acetate, ethanol and n-propanol are produced by slight decomposition of the carbon cloth electrode

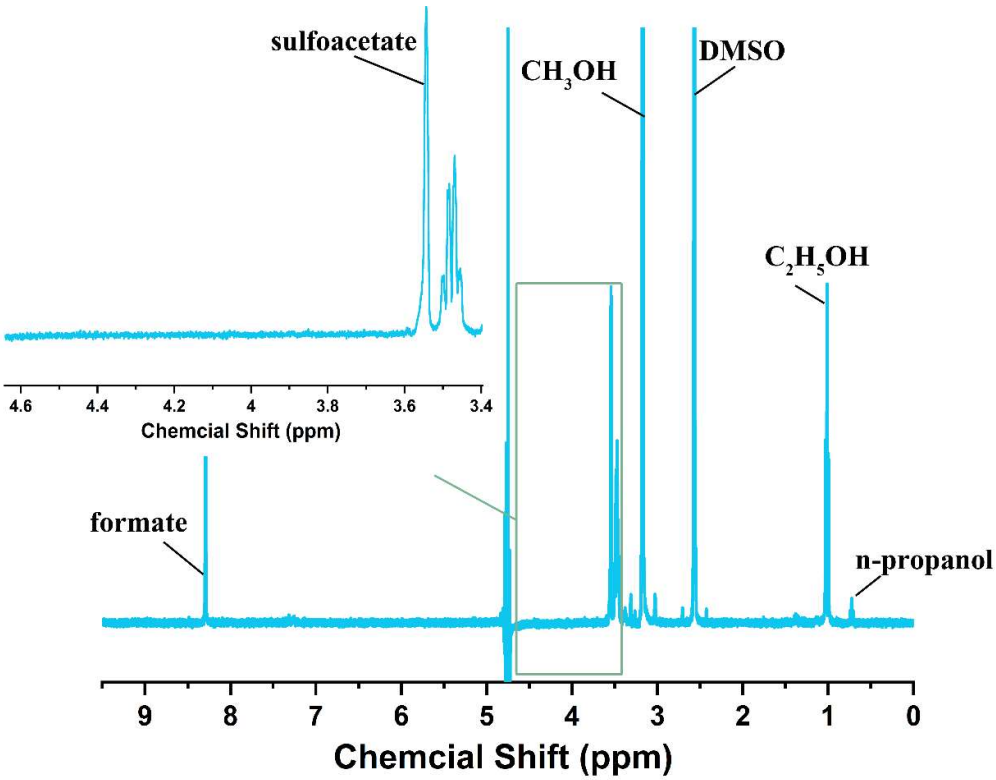

Figure S13. Formaldehyde (HCHO) was used as substrate instead of CO_2 to conduct electrolysis in 1M KOH + 0.2 M Na_2SO_3 at -1.08 V. No signal of HMS was observed, which suggests that HCHO is not the intermediate for HMS formation.

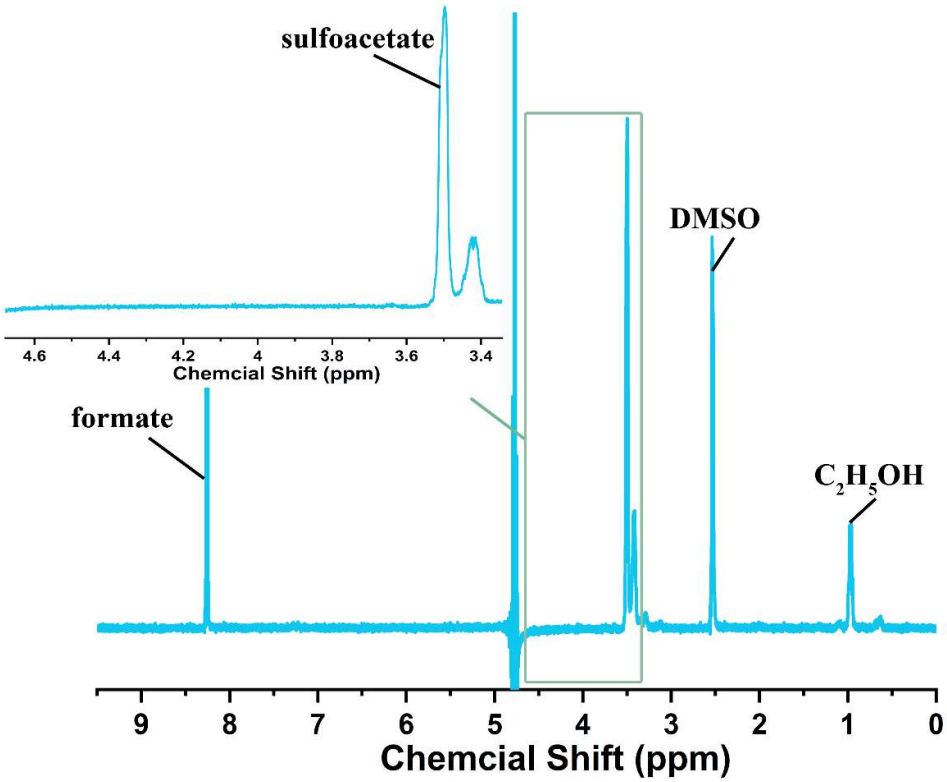

Figure S14. Formate was used as a precursor to replace CO_2 to conduct electrolysis. The reaction condition is the same as the CO_2RR reaction, in which the electrolyte is 1 M KOH + 0.2 M sulfite, under -0.68 V. There is no HMS obtained after reaction, which suggests that formate is not the intermediate for HMS production.

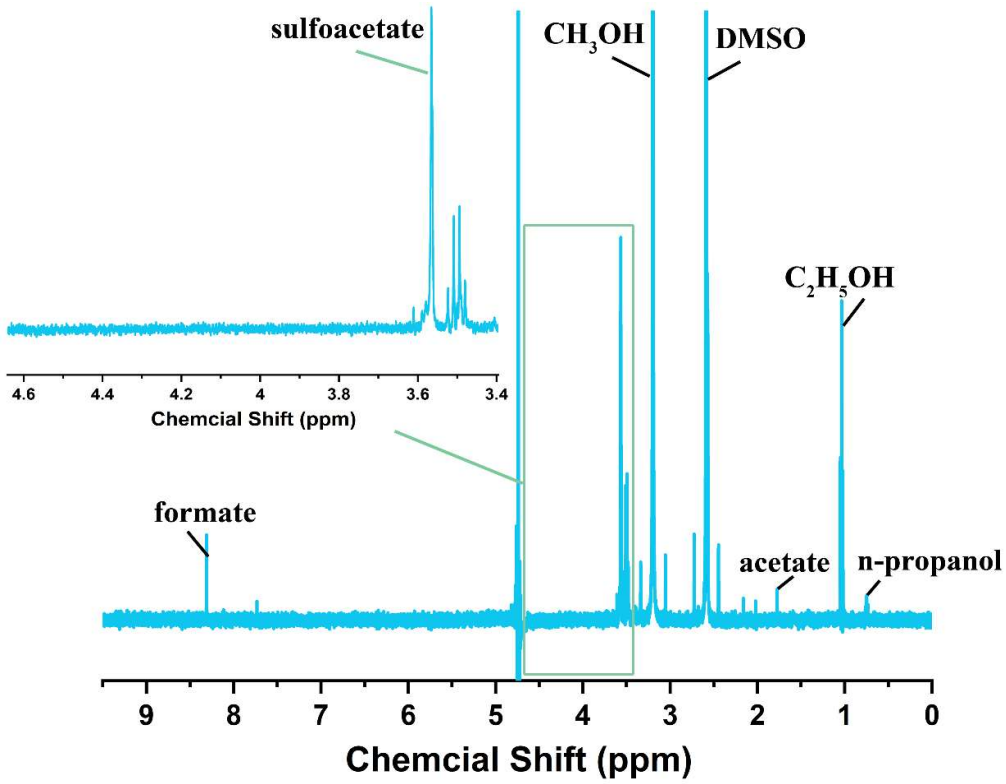

Figure S15. Methanol was used as a precursor instead of CO_2 for C-S coupling. The reaction condition is the same as the CO_2RR reaction, in which the electrolyte is 1 M KOH + 0.2 M sulfite, under -1.08 V. Also, there is no CH_3NaO_4S obtained after reaction, which suggests that HMS is not the intermediate for HMS production.

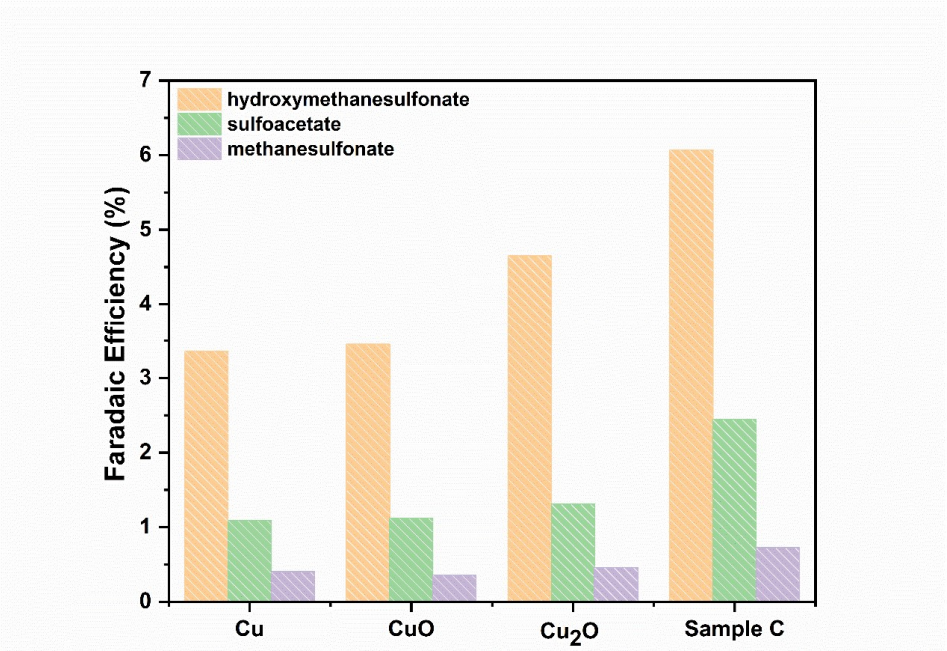

S16. Comparison of C-S product formation under optimized conditions (-0.68 V vs. RHE, 1 M KOH, 200 mM SO_3^{2-}) of synthesized and commercially purchased Cu catalysts.

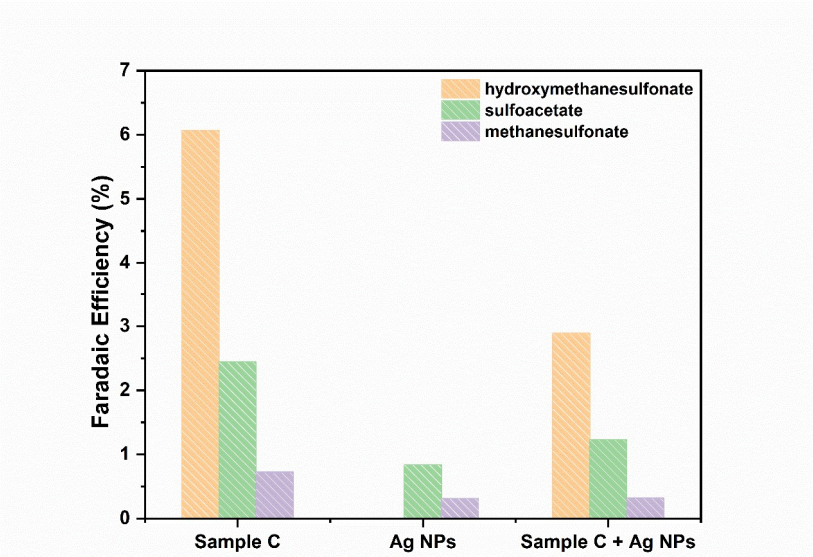

Figure S17. HMS and SA formation with Ag nanoparticles (NPs) used as catalysts under the optimized conditions of 0.2 M Na_2SO_3, 1.0 M KOH and -0.68V_{RHE}.

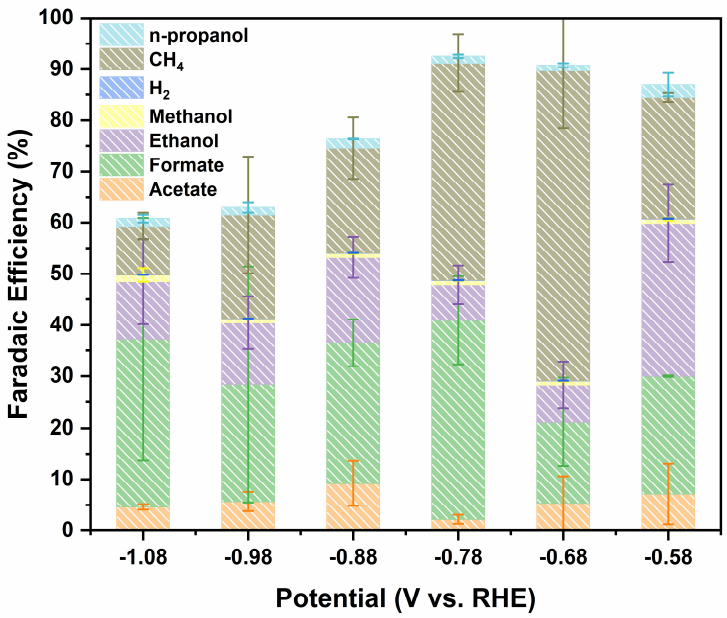

Figure S18. Faradaic efficiencies for the electrochemical system in the absence of SO_3^{2-}, using the optimized catalyst C in 1.0 M KOH and CO_2 flow.

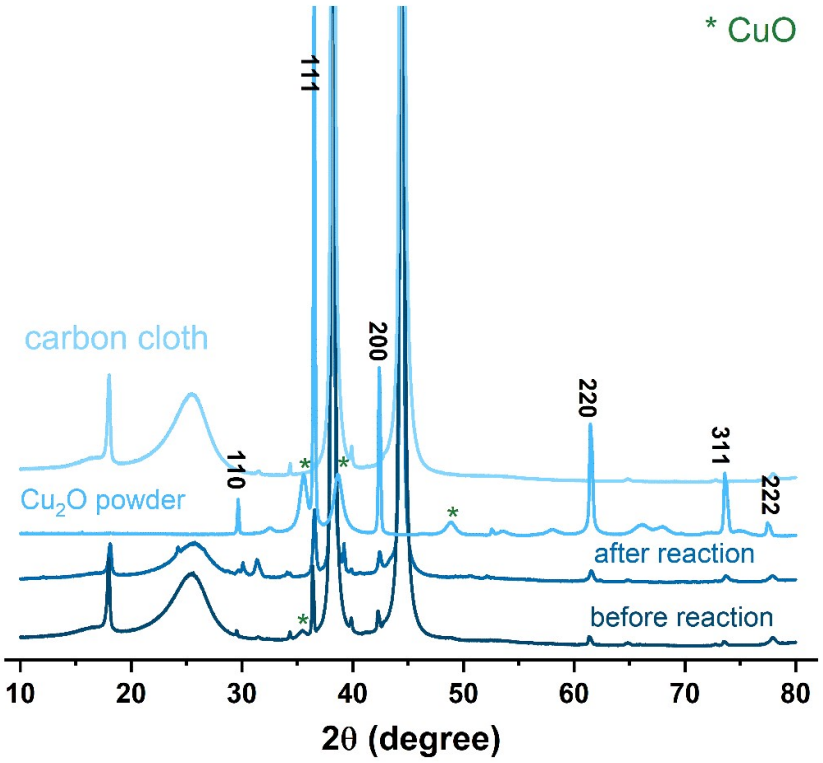

Figure S19. XRD patterns of sample C powder, bare carbon cloth, working electrodes with sample C before and after reactions. Comparing these patterns, sample C electrode shows the peaks at 18.01°, 25.28°, 38.27°, and 44.41° belong to graphite. Before reaction, sample C contain Cu_2O (JCPDS card no. 05-0667), (110), (200), (220), (311) and (222) signals were observed at 29.55°, 42.30°, 61.34°, 73.53°, and 77.32°, respectively. Besides these peaks, 2θ values of 35.54°, 38.71°, and 48.72° could be indexed to (11-1) and (111), (20-2) planes of CuO (JCPDS card no. 48-1548). After the reaction, peaks of graphite and Cu_2O are observed, but peaks of CuO are missing.

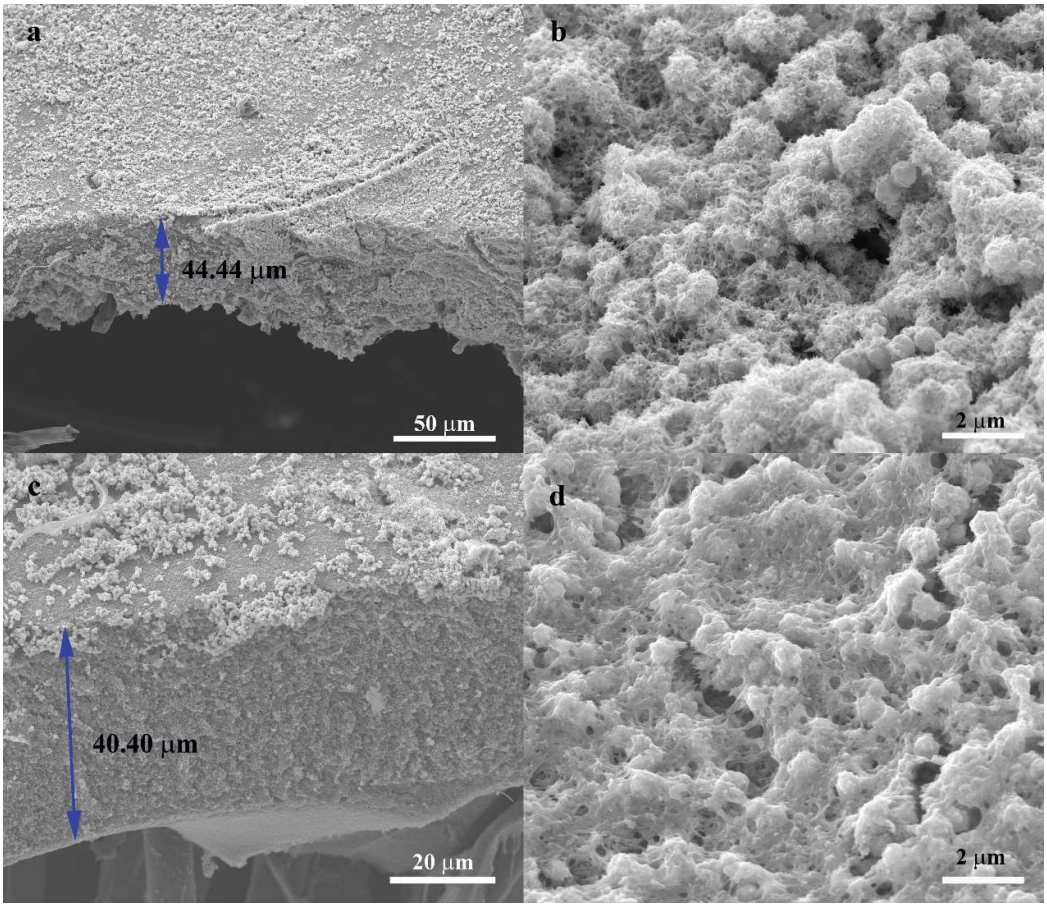

Figure S20. SEM images of sample C. (a) cross session and (b) electrode surface before reaction; (c) cross session and (d) electrode surface after reaction.

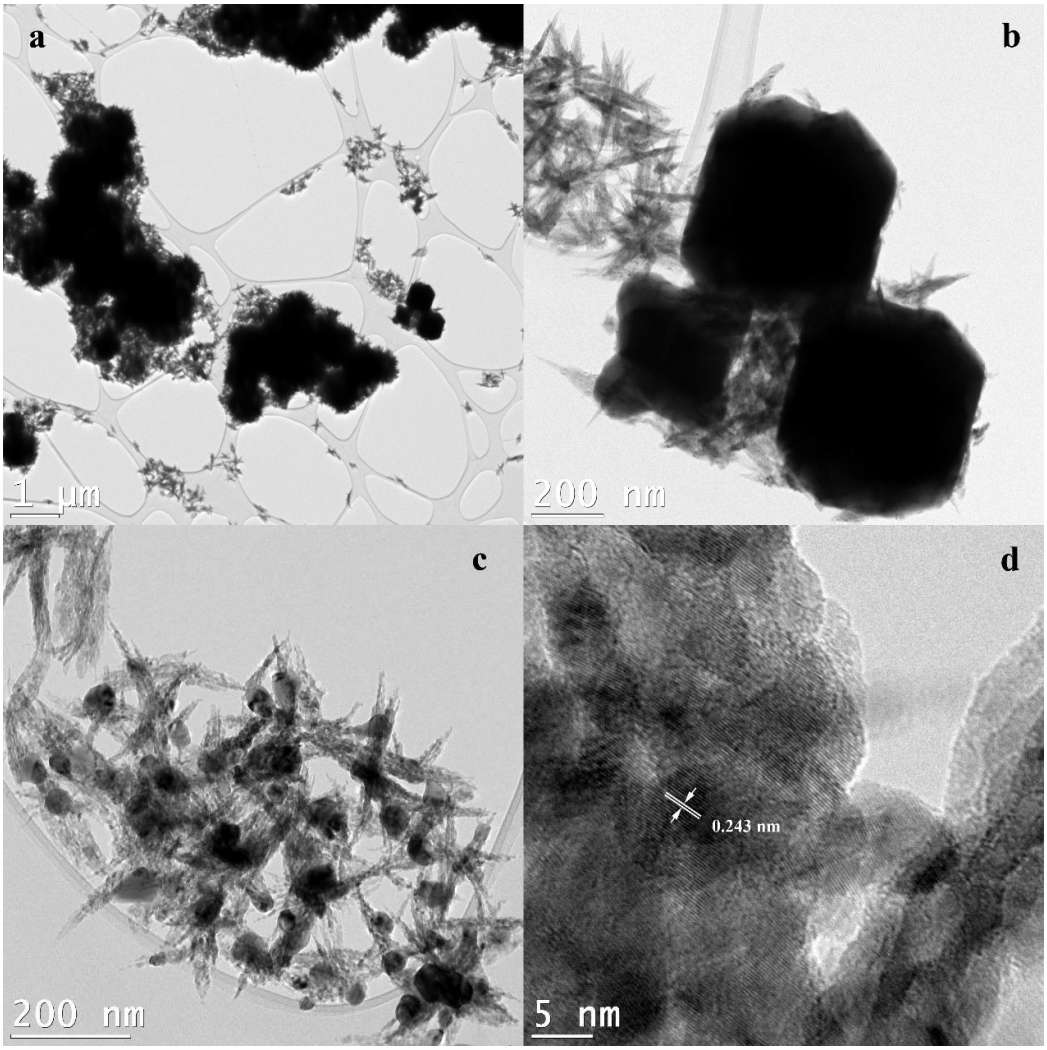

Figure S21. (HR)TEM images of sample C powder before the reaction. The morphology is consistent with SEM results, which is the mixture of incompletely grown octahedron and sea urchin particles constituted by short nanowires. Nanowires are formed by the aggregation of small nanoparticles. The lattice distance of 0.243 nm could be attributed to the Cu_2O (111) planes.

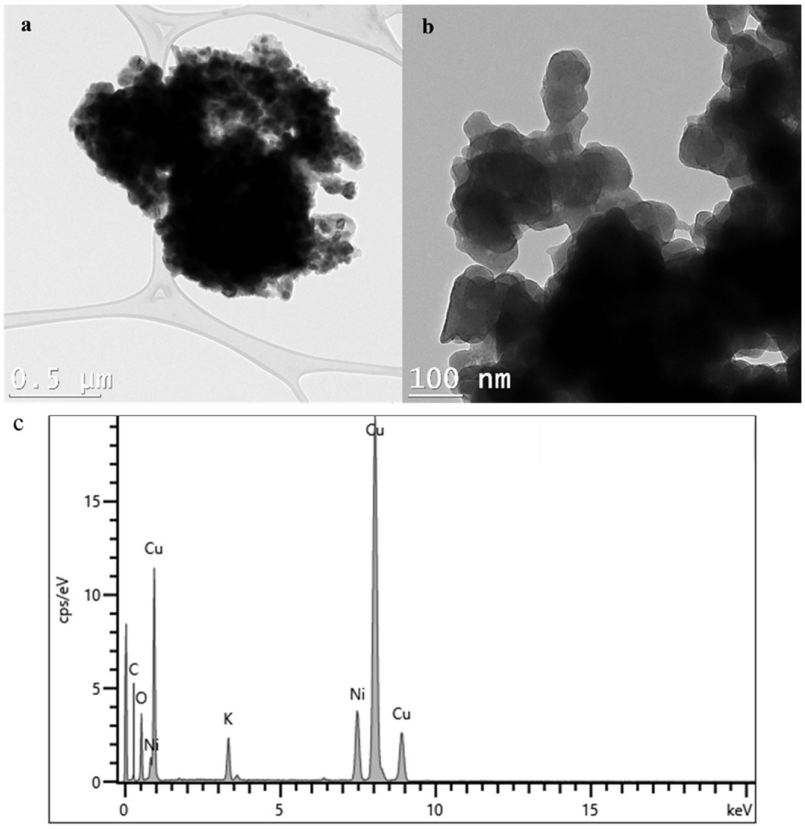

Figure S22. (HR) TEM images of sample C after catalysis (1 hr at -0.68V vs. RHE). The samples are scratched from carbon cloth electrode onto a Ni TEM grid. Short nanowire-like features disappear, and small nanoparticles are further aggregated to form larger nanoparticles (a, b). EDS analysis shows that Cu and O are the main elemental components of the particles. Traces of S can occasionally be seen at 2.5 keV.

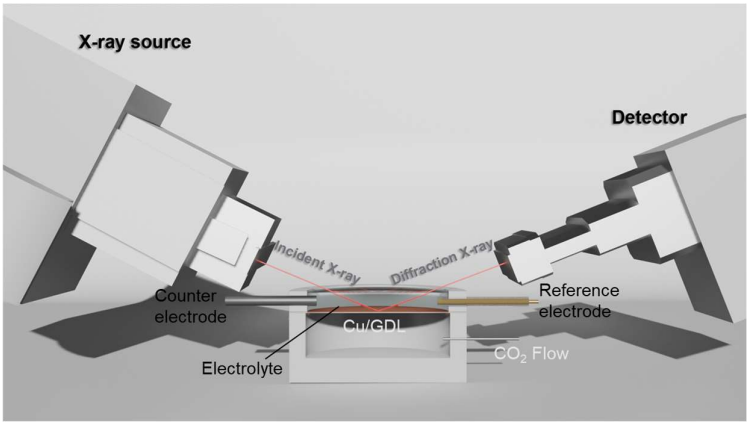

Figure S23. Schematic of *operando* XRD measurement setup.

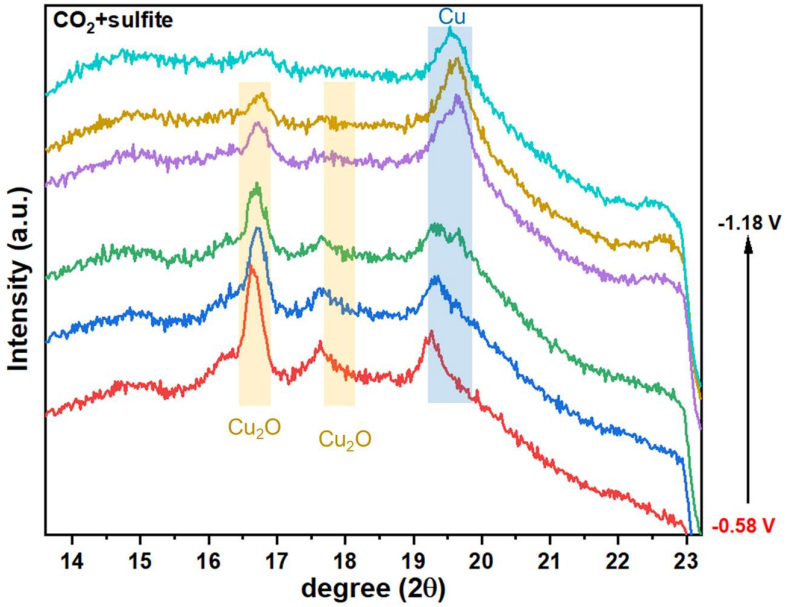

Fig. S24. *Operando* XRD experiments (Mo source) carried out as a function of applied potential (vs. RHE) with 1 minute per potential. Within 5-6 minutes of reducing potential, the Cu_2O (16.5° and 18°) and CuO (19.5^0) largely disappear, and metallic Cu is the main crystal phase observed.

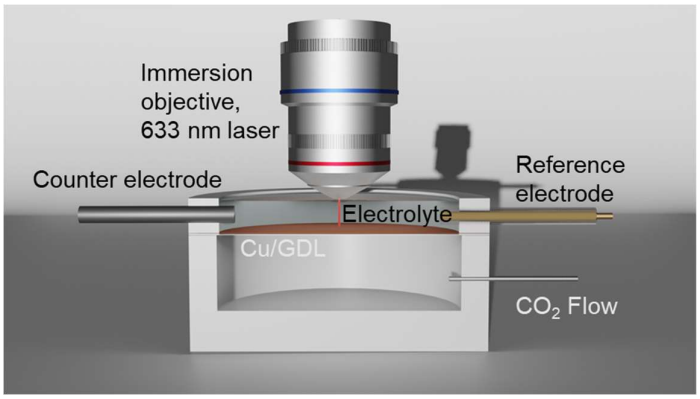

Figure S25. Reaction cell used for *operando* Raman measurements under CO_2 flow and a gas diffusion layer as a working electrode.

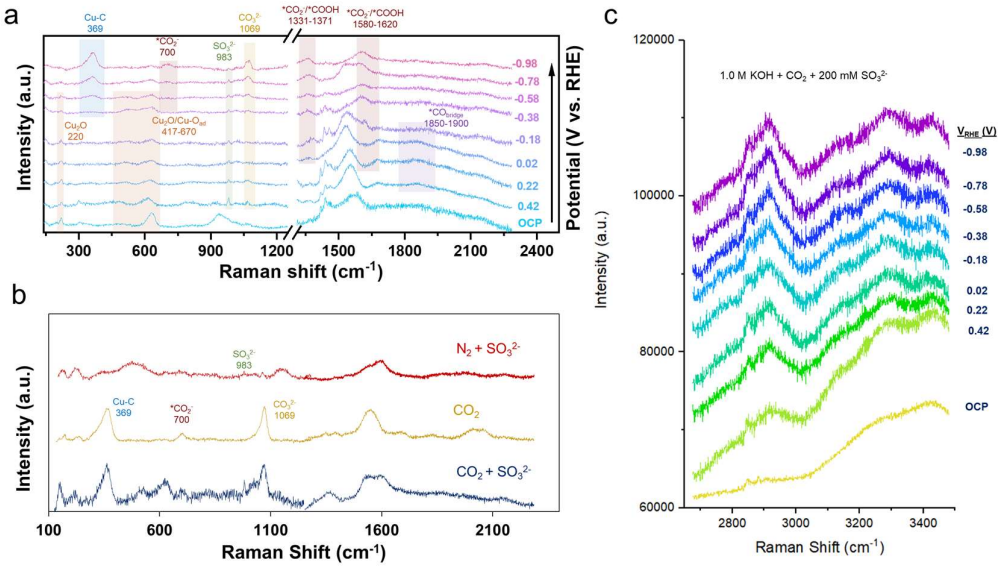

Figure S26. High and low-frequency Raman spectra under typical C-S coupling conditions (a) and comparison of Raman spectra of the Cu catalyst at -0.78V_{RHE} with CO_2 only and SO_3^{2-} only (b). C-H stretches around 2800-2900 cm^{-1} are also evident under C-S bond forming conditions (c).

Table S2. Adsorption energies of two sulfur compounds and three copper surfaces

Adsorption energies	**100**	**110**	**111**
SO_3^{2-}	0. 87 eV	0.49 eV	1.54 eV
HSO_3^-	1.74 eV	1.48 eV	2.02 eV

Table S3. Energies of optimized copper slabs

Size	**Surface**	**Energy (a.u)**	**Energy (eV)**
$5 \times 5 \times 4$	100	-4811.5	-130926
$5 \times 5 \times 4$	111	-4811.7	-130933
$5 \times 5 \times 4$	110	-4810.9	-130910

Table S4. Energies of adsorbed intermediated on Cu (100) and isolated molecules

Intermediate	**Energy (a.u)**	**Energy (eV)**	**Position**
CO	-4833.226	-131517	Bridge C*
CHO	-4833.793	-131532	Bridge C*+Top O*
COH	-4833.784	-131532	Hollow C*
CHOH	-4834.371	-131548	Bridge C*
CH_2O	-4834.400	-131549	Bridge C* + Bridge O*
CH_2OH	-4834.985	-131565	Top C* + Top O*
HMS (-)	-81.649	-2221.74	Deprotonated (-1 charge)
HMS	-82.348	-2240.77	Protonated (0 charge)
SO_3CO	-4891.507	-133103	Stays connected
$HOSO_2CO$	-4892.113	-133119	Disconnected, unfinished
SO_3COH	-4892.088	-133119	C*, connected
SO_3CHO	-4892.103	-133119	CHO on top of SO_3 by C* on S
SO_3CHOH	-4892.697	-133135	C*, connected
SO_3CH_2OH	-4893.314	-133152	SO3*, CH2OH lifted up
SO_3CH_2O	-4892.699	-133135	CH2O desorbs, unfinished
$HOSO_2CH2OH$	-4893.872	-133167	Desorbs, Unfinished
$HOSO_2CHO$	-4892.700	-133135	Separated
$HOSO_2CHOH$	-4893.264	-133151	C*, Connected
$HOSO_2COH$	-4892.659	-133134	C*
HSO_3	-58.929	-1603.53	Individual molecule
$H2SO_3$	-59.452	-1617.74	Individual molecule

HSO_3+CHOH	-4893.272	-133151	Surface coupling
HSO_3+ COH	-4892.689	-133135	Surface coupling
SO_3+CHOH	-4892.692	-133135	Surface coupling
SO_3+COH	-4892.108	-133119	Surface coupling

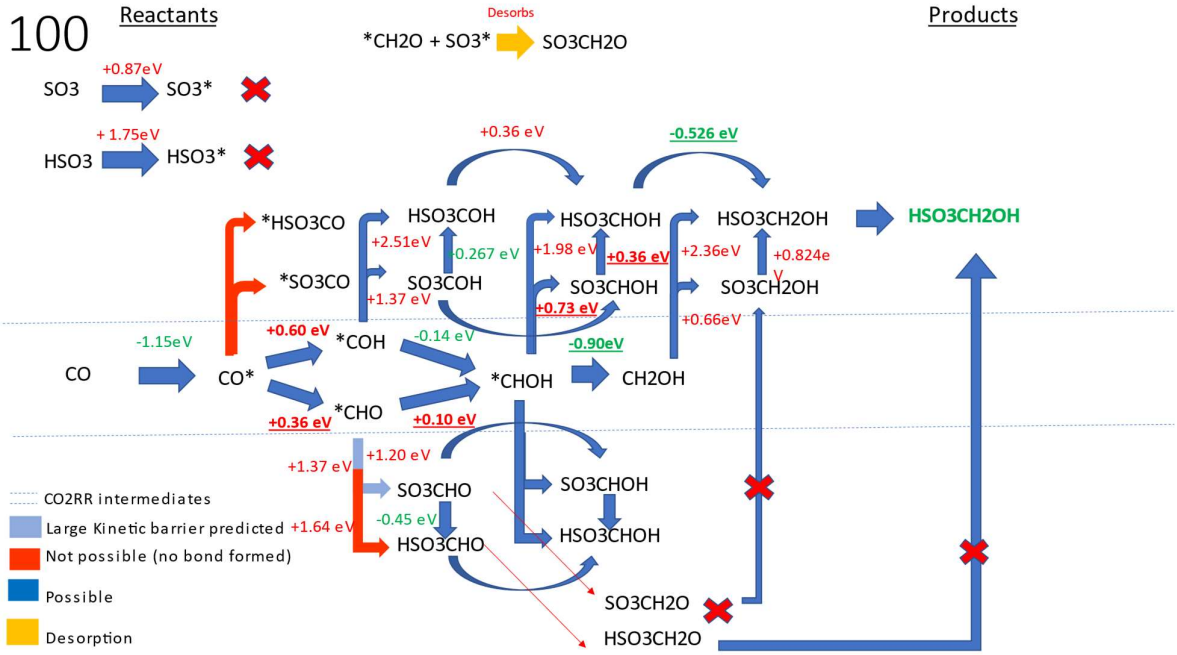

Figure S27. Reaction pathway from CO to HMS on Cu (100) including energy barriers, adsorption energy. Underlined values show the most promising pathway. Red values are positive while green values are negative energy barriers

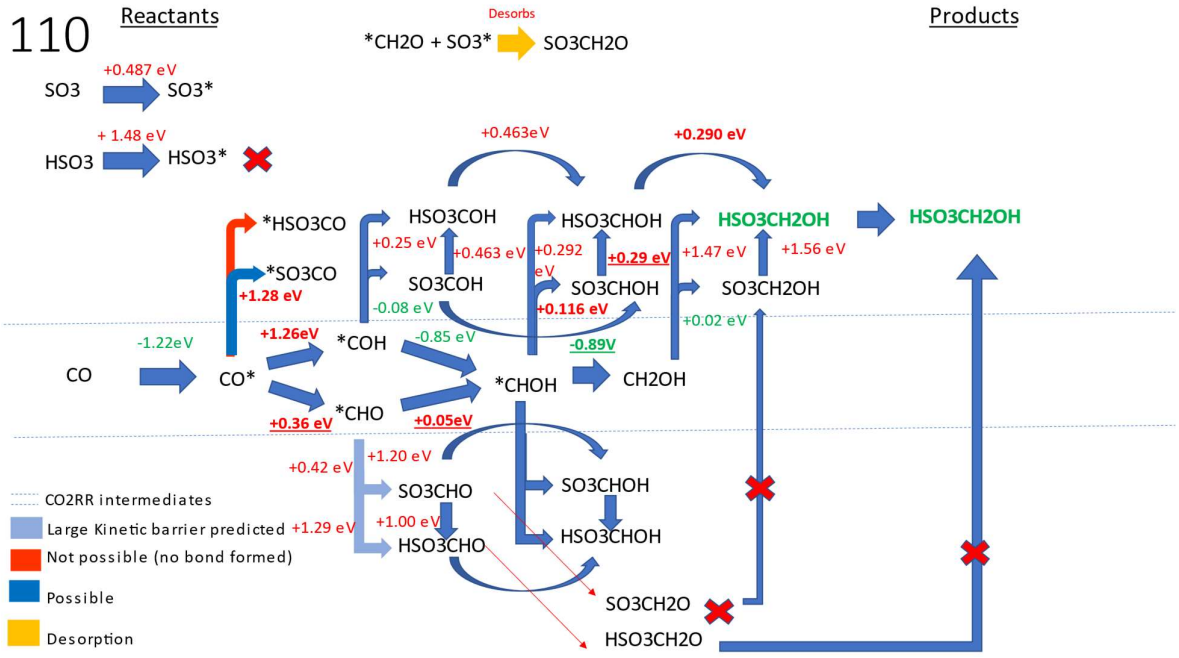

110 energy barrier and pathway

Figure S28. Reaction pathway from CO to HMS on Cu (110) including energy barriers, adsorption energy. Underlined values show the most promising pathway. Red values are positive while green values are negative energy barriers

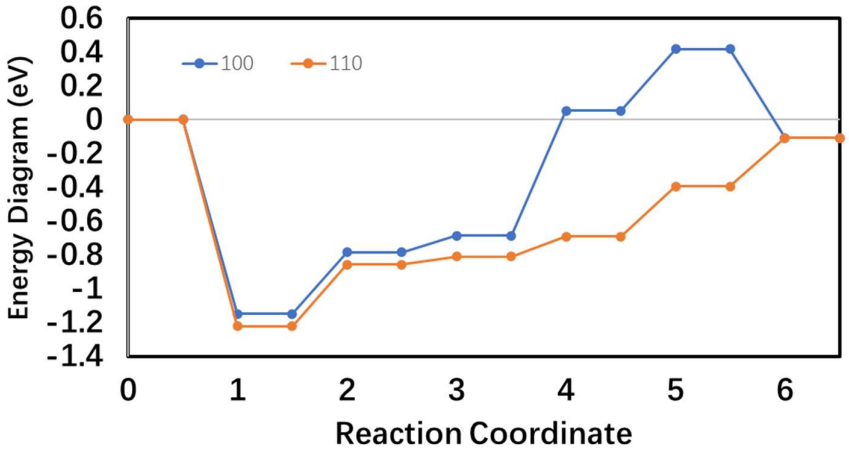

Figure S29. Comparing energy diagrams of (100) and (110)

Table S5. Comparison of energy barriers and coupling barriers of Cu(100) and Cu(110)

	Main coupling step	Coupling barrier	RDS barrier (eV)	RDS
100	SO_3+CHOH	0.740	**0.74**	SO3+CHOH => SO3CHOH
110	SO_3 +CHOH	0.116	**0.36**	CO=>CHO

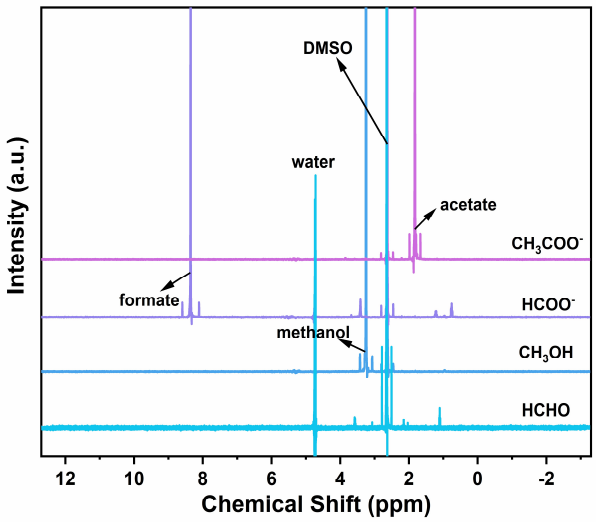

Figure S30. 200 mM carbon reactants were mixed with 200 mM SO_3^{2-} in 1M KOH for more than 24 hrs and potential formation of products was monitored for by NMR. No HMS, SA or MS would be observed within our typical sensitivity limits.

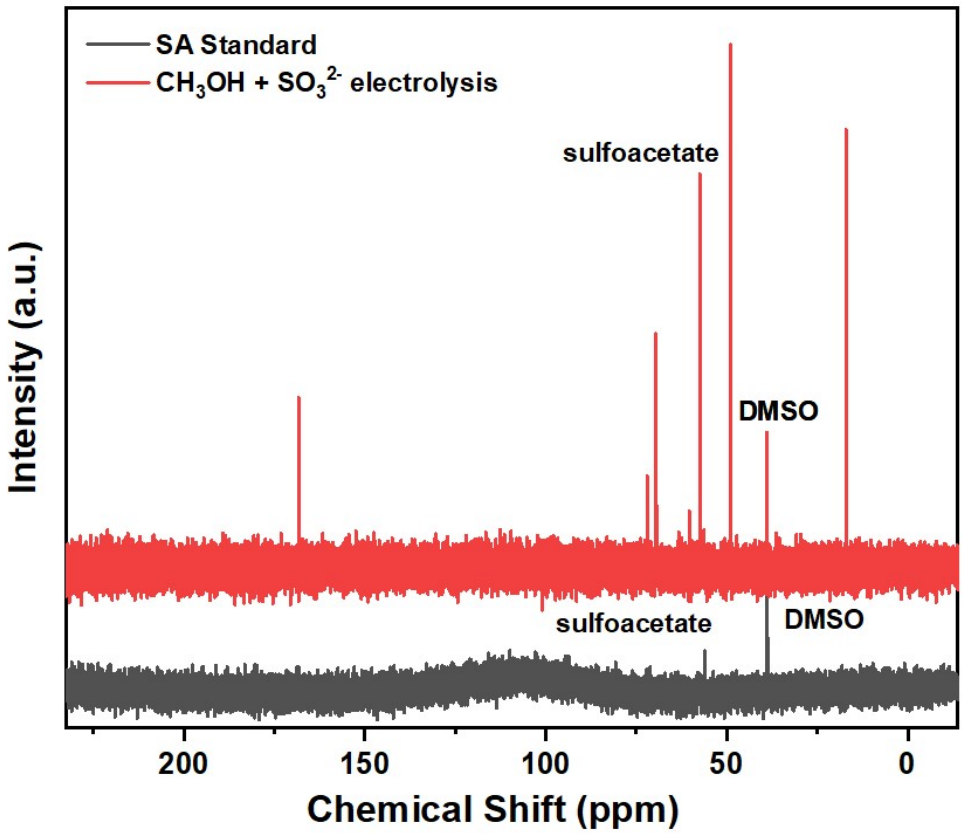

Figure S31. ^{13}C NMR of sulfoacetate after 30 min of co-electrolysis with CH_3OH and SO_3^{2-}.

References:

1. J.-Y. Ho and M. H. Huang, *The Journal of Physical Chemistry C*, 2009, **113**, 14159-14164.